

Parametric and Generative Forecasts of Day-Ahead Market Curves for Storage Optimization

Julian Gutierrez^a, Redouane Silvente^a

^a*CREST, ENSAE, Institut Polytechnique de Paris, 5 Avenue Henry Le Chatelier 91120 Palaiseau, France*

Abstract

We present two machine learning frameworks for forecasting aggregated curves and optimizing storage in the EPEX SPOT day-ahead market. First, a fast parametric model forecasts hourly demand and supply curves in a low-dimensional and grid-robust representation, with minimum and maximum volumes combined with a Chebyshev polynomial for the elastic segment. The model enables daily use with low error and clear interpretability. Second, for a more comprehensive analysis, though less suited to daily operation, we employ generative models that learn the joint distribution of 24-hour order-level submissions given weather and fuel variables. These models generate synthetic daily scenarios of individual buy and sell orders, which, once aggregated, yield hourly supply and demand curves. Based on these forecasts, we optimize a price-making storage strategy, quantify revenue distributions, and highlight the price-compression effect with lower peaks, higher off-peak levels, and diminishing returns as capacity expands.

Keywords: Day-ahead electricity market, Aggregated supply and demand curves, Chebyshev approximation, Conditional diffusion model, Marked point process, Storage optimization, Price impact, JEL: C45, C53, Q41, Q47

1. Introduction

According to the International Energy Agency (IEA)¹, in a context of massive electrification of our lifestyles, global electricity consumption increased by 4.3 % in 2024, well above the 2.5 % recorded in 2023. In France, Réseau de Transport d’Électricité (RTE)² forecasts roughly a 35 % rise in demand by 2050. This increase is already beginning to show up on the European Power Exchange Spot Market (EPEX SPOT), where, between 2023 and 2025, the volume of energy traded climbed by nearly 60%, from 542 TWh to 868 TWh. This short-term electricity market is made up of two main segments: the larger is the day-ahead market, which accounted for 654 TWh in Europe in 2024³ and which is the focus of this work. The second is the intraday market, which reached 215 TWh in 2024. This growth occurs in parallel with an increase in the number of traders, which may result in more complex orders.

On the day-ahead market, price formation follows the merit-order principle. Before 12:00 on day J , traders and consumers must submit their buy and sell bids for every hour of day $J+1$ to EPEX SPOT. Sell bids are then aggregated in ascending order of price, and buy bids in descending order. The intersection of these two curves, known as the market-clearing price, becomes the day-ahead

¹This work has been carried out at the Energy4Climate Interdisciplinary Center (E4C) of IP Paris, which is in part supported by 3rd Programme d’Investissements d’Avenir [ANR-18-EUR-0006-02], and by the Foundation of Ecole polytechnique (Chaire “Décarboner l’économie” financed by BNP Paribas).

²Corresponding author: Julian Gutierrez (julian.gutierrezpin@gmail.com)

Email addresses: julian.gutierrezpin@gmail.com (Julian Gutierrez), redsilvente@gmail.com (Redouane Silvente)

¹<https://www.iea.org/reports/global-energy-review-2025/electricity>

²<https://rte-futursenergetiques2050.com/trajectoires/trajectoire-de-reference>

³<https://www.epexspot.com/en/news/annual-trading-results-2024-power-trading-epex-spot-reaches-all-time-high>

electricity price. An example of merit-order is displayed in Figure 1. There are three types of participants. The first category comprises those active solely on the supply side: producers (coal, gas, or nuclear power plants, and renewable energy generators) who offer for sale the quantities of energy they can produce. The second category consists of electricity suppliers: companies that deliver energy to end-users, whether households or small and medium-sized enterprises. Some large corporations and major industrial sites also manage part of their own consumption directly in the day-ahead market. There are also flexibility operators, who participate exclusively on the demand side. Finally, the third category includes agents active on both the demand and supply sides. These may be pure traders (banks, hedge funds) or storage operators, who time their purchases and sales optimally according to their capacity constraints.

On EPEX SPOT in the day-ahead market, it is possible to submit block orders that are executed only when certain conditions are met. For example, a participant may place a buy order only if they are sure they can resell it later the same day. Consider an agent owning a storage asset: if this agent is too small to influence the price (i.e., a price-taker), it suffices to optimize the spread by selecting one off-peak hour and one peak hour and arbitrage by injecting as much energy as possible. In the case of a price-maker agent, however, one must account for the possibility that storing too much during the off-peak hour and selling too much during the peak hour could drive the spread negative, rendering the operation unprofitable. This balance is delicate to find and requires forecasting both the supply and demand curves for each hour of the next day. Predicting these two curves has two main uses: on the institutional side, where many challenges remain for Transmission System Operators (TSOs) in their forecasts (Kazmi and Tao (2022)), and for traders seeking to optimize their market strategies. These two needs come with different constraints. For a trader, the requirement is to have a prediction that can be produced quickly, every day, to set their strategy at $J - 1$ before noon. However, a deeper study of the electricity market requires traders to analyze both the robustness of their strategies and their impact on market dynamics. This aligns with the objective of a TSO, which prioritizes a deeper understanding of market uncertainty, even at the cost of the faster performance offered by previous methods. This work addresses this dual problem by focusing on the modelling and generation of realistic aggregated supply and demand curves for each hour of the day-ahead market, rather than on direct price forecasting. Although prices may emerge endogenously as curve intersections, they are not the primary target. This curve-based approach is essential for analysing price-maker storage agents, whose decisions depend on how their bids reshape the merit order. The resulting curve representations are therefore designed as inputs to a storage optimization problem, enabling the assessment of price impact, profitability, and risk under market uncertainty.

In the first section of our work, we develop a prediction method with XGBoost that is sufficiently fast for daily use. The main difficulty arises from the fact that, for each delivery hour, the demand and supply curves are defined on different (Price, Volume) grids. The key observation is that the curves exhibit a similar shape every day. For instance, regarding demand, this approach allows us to reduce the problem to predicting only eight parameters: the minimum quantity required to ensure system reliability, the maximum quantity the system can accommodate, and in between, a polynomial approximation of the elastic portion of the demand curve for each delivery hour. The process is the same for the supply curves. This fast-running model achieves a normalized mean absolute error of about 8-11% relative to the original curves. Although higher than what slower, heavily tuned curve fitting approaches often report, our goal is operational usability and economic consistency: an interpretable, monotonic, grid-robust representation that jointly forecasts supply and demand and is usable by a trader on a day-to-day basis. This model serves as a baseline for our subsequent bid-level generative approach.

Once this short-term prediction is achieved, the second objective of our work is to address the longer-term problem, which remains useful not only for traders but also for TSOs. As renewable penetration increases, underlying fundamentals (weather-driven supply, fuel price shocks, and network constraints) introduce significant volatility. As a result, forecasting best practices now emphasize probabilistic approaches that quantify uncertainty rather than relying solely on point estimates. This second approach trades speed for depth: it is less suitable for day-to-day $J - 1$ operations but enables

a more thorough analysis. To implement it, we turn in Section 3 to Denoising Diffusion Probabilistic Models (DDPMs). This class of generative models is characterized by an iterative noise-removal process that gradually reconstructs samples from pure noise, thereby learning to encode the underlying data distribution. This mechanism allows the model to capture complex dependencies, a key requirement for representing the weather- and fuel price-driven volatility characteristic of European electricity markets. To model supply and demand curves, we decompose them into marked Point Processes, generating each offer that composes the curve. The procedure is conducted in two stages: first, the submission prices of the offers are generated; second, the corresponding offer volumes for the 24 hours of the day are drawn, conditional on these prices and on additional weather and fuel price variables. Across generated samples, the generative model attains an average normalized mean square error of approximately 1.3-5% relative to the original curves. This offer-level approach to one-day forecasting captures the distribution of possible market outcomes and generates curve samples that reproduce the shapes observed in the market. Since the method requires only weather and fuel price variables as inputs—*independent* of past supply and demand data—it can also be extended beyond the daily horizon: by aggregating samples across multiple days, we can perform long-term scenario analyses.

Our objective in developing these two modelling frameworks is not to benchmark predictive accuracy against existing methods, but to construct tractable and internally consistent curve representations that can be integrated into a downstream optimization problem. Accordingly, once the demand and supply forecasts have been obtained, Section 4 investigates the optimal strategy of a price-maker storage agent in the day-ahead market, operating between one charging and one discharging hour. We adopt two complementary forecasting approaches. The fast parametric baseline model provides predictions suitable for daily use. It enables the evaluation of storage revenues, which we compare against a naïve benchmark to demonstrate performance. In contrast, the generative model produces probabilistic scenarios, which, although too costly to deploy daily, allow for a deeper assessment of price impact, capacity value, and stress testing. Using these forecasts, we first quantify the distribution of revenues that a storage agent can anticipate for a given date and then measure the effect of storage operations on electricity prices, highlighting their spread-compression role. Finally, we show how the generative scenarios enrich this baseline by providing robustness and sensitivity analyses of storage profitability.

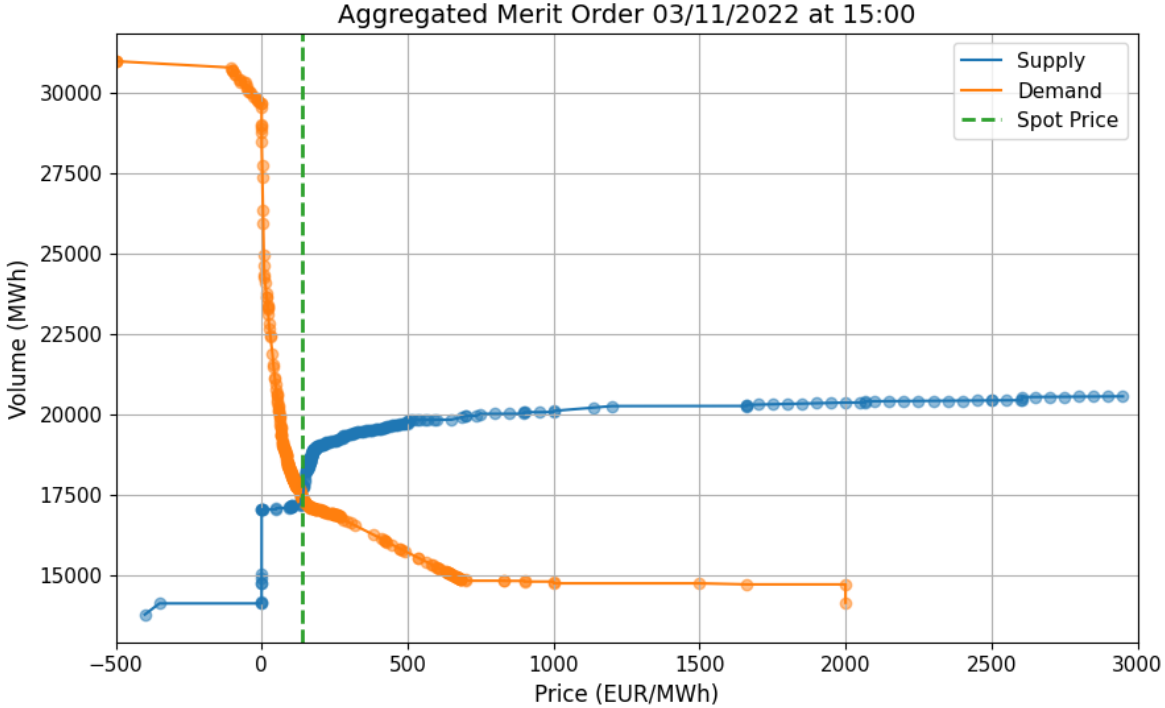


Figure 1: Aggregated bid and offers for 2022-11-03 at 3pm. The Demand curve, including an elastic part, is in orange and the Supply curve is in blue. They cross at the day-ahead electricity price.

Our results show that accounting for price impact fundamentally changes the profitability profile of storage. Compared with a naïve strategy that ignores its own market influence, a price-maker storage avoids negative revenues and achieves higher average profits. Beyond individual revenues, storage operation compresses spreads by reducing peak prices and raising off-peak levels, consistent with the literature on flexibility. These findings are in line with Dumitrescu et al. (2024), which documents a similar compression effect in the intraday market. In both cases, increasing storage capacity initially improves profitability, but marginal gains diminish rapidly due to a cannibalization mechanism: the more storage is deployed, the less value each additional unit provides relative to its capacity, leading to very long payback times. This highlights both the stabilizing role of storage for the market and the limits of its scalability under current cost structures.

The paper is structured as follows. In the rest of this Section, we review the relevant literature. Section 2 presents the prediction of demand and supply curves with the fast parametric model, while Section 3 develops the generative bid-level model. Finally, the application to storage optimization is done in Section 4.

Literature review. The prediction of demand and supply curves originally emerged as a type of price forecasting model. Barlow (2002) is one of the first works motivated by real data, using stochastic models for demand and supply. In this line of research, the emphasis is on constructing explicit representations of supply and/or demand curves, from which prices are subsequently obtained as their intersection. This perspective aligns with our objective of building realistic, data-driven representations of aggregated bid curves for storage optimization, and motivates our focus on curve-based modeling approaches rather than price-only forecasting models.

Within this framework, Buzoianu et al. (2005) specifies latent, time-varying supply and demand curves in a nonlinear state-space with exogenous drivers and estimates the model via particle filtering to obtain one-step-ahead predictive distributions for prices and quantities, rather than explicit curve forecasts. Explicit curve forecasting appeared later: Aneiros et al. (2013) model residual demand as

a functional time series, comparing a functional nonparametric autoregression with a semi-functional partial linear model using wind and load forecasts, while Canale and Vantini (2016) forecast gas offer and demand curves with a constrained (penalized) functional autoregression.

A significant difficulty is that supply and demand curves are not defined on a shared price–volume grid across hours, as each hourly curve is supported by its own set of price-volume points. As a result, curves from different hours are not directly comparable. A standard approach in the literature is therefore to impose a fixed grid shared across all hours, providing a common support on which hourly curves can be represented and analysed jointly. The well-known paper by Ziel and Steinert (2016) adopts this approach in the X-model, developed within an econometric framework. See also Shah and Lisi (2020) and subsequent extensions of the X-model Haben et al. (2021); Kulakov (2020), which incorporate exogenous variables such as temperature and wind. Some papers focus on supply prediction while assuming demand is inelastic (e.g., Mitridati and Pinson (2017); Kulakov (2020)). In this case, the goal is essentially price forecasting, not an accurate representation of the entire curve. More recently, Ghelasi and Ziel (2024) extends the X-Model by combining class-wise LASSO regressions with hierarchical reconciliation to ensure consistency between marginal and cumulative curves, improving curve accuracy while remaining an econometric approach. Beyond econometric methods, machine learning is also applied to forecast curves, for instance in Guo et al. (2021) where the authors use an LSTM reaching a high point accuracy. However, they forecast only the aggregated supply curve but do not provide a demand curve; their approach has low interpretability and heavy preprocessing. Foronda-Pascual and Alonso (2023) focuses on supply curves and proposes a two-step curve-based forecasting approach that maps all curves onto a common fixed price grid, casting the problem as multivariate prediction. Using lagged curves, calendar effects, market variables, fuel prices, and weather indicators, the full supply curve is forecast via machine-learning methods, with Histogram-Based Gradient Boosting yielding the best performance.

Another approach is to change the representation of curves. For instance, Li et al. (2025) forecasts both curves functionally, but uses about 50 coefficients per curve on a fixed price grid and a post-processing step that replaces each prediction by its closest historical curve to restore monotonicity. Our first fast prediction model forecasts supply and demand in a low-dimensional, monotone, grid-robust, and interpretable form. It aims to reduce the complexity of curve prediction, making it more usable in practice compared to a full-grid prediction. We build on recent methods that represent each curve with a finite set of parameters. In Ciarreta et al. (2023), the elastic part is approximated with logistic or linear functions. In Soloviova and Vargiu (2020), curves are represented via integrals of radial basis functions. In the recent paper Sinha and Lucheroni (2025), curves are split into three zones defined by fixed prices, with the central zone capturing elasticity. We combine these ideas by modelling demand and supply curves with an elastic part through a polynomial approximation and two plateaus, and additionally forecasting the price bounds of the elastic section. This machine learning approach captures the specific shape of aggregated bid curves while massively reducing complexity.

This approach, however, fails to capture the specific randomness inherent in demand, renewable production, and electricity markets, which is necessary for more in-depth analysis. The DDPMs we employ in Section 3 provide a powerful alternative for modeling supply and demand. This class of generative models has already shown strong performance in probabilistic energy time-series (load, photovoltaic (PV), wind) and scenario generation. For example, Capel and Dumas (2023) generates full daily load, PV, and wind series conditioned on weather forecasts, outperforming Generative Adversarial Networks (GANs), Variational Autoencoders (VAEs), and Normalizing Flows (NFs) when evaluated with both statistical scores and market-based measures such as day-ahead bidding and storage scheduling. Li et al. (2024) adapts diffusion models with self-attention to generate electric vehicle (EV) charging demand, validated through statistical distances and bidding simulations. Lin et al. (2024) demonstrates scalability to high-resolution time series (up to minute-level) and introduces marginal calibration via optimal transport. Zhang et al. (2024) proposes a physics-informed diffusion model integrating PV system performance for net load generation. Complementing these applications, Han et al. (2024) provides theoretical guarantees for neural-network-based score estimation in diffusion processes. These works establish DDPMs as state-of-the-art generative tools for realistic scenario gen-

eration in electricity markets, especially for supply-demand modelling. To the best of our knowledge, this is the first work to model day-ahead auction supply and demand curves at the bid level and to generate such bids using DDPMs.

Our paper then proposes a complete framework to study the optimal strategy of a storage agent in the day-ahead electricity market. Most existing works on storage assume a price-taker setting (Mercier et al. (2023); Aazami et al. (2022); Collet et al. (2017); Dumitrescu et al. (2024)), focusing on optimal strategies under physical and price constraints. For a broader review of storage optimization, see Machlev et al. (2020) and the introduction in Dumitrescu et al. (2024).

In contrast to the existing literature on price-taking storage in day-ahead markets, we study the less common case of a price-maker storage in the day-ahead market. This case appears in Ding et al. (2017), which models uncertainty via scenarios but assumes known curves; in Biggins et al. (2022), which compares price-taker and price-maker strategies; and in Shafiee et al. (2016); Barbry et al. (2019). In these works, supply and demand curves are either assumed known or reconstructed from historical data without being embedded in an explicit modeling framework. We build on Supply Function Equilibrium (SFE) models (see Klemperer and Meyer (1989); Anderson (2013); Baldick et al. (2004); Holmberg and Newbery (2010)), which have also studied the case of capacity constraints (Holmberg (2008)). In our setting, the storage optimizes block orders across hours, with decisions based on price. To our knowledge, this is the first work to jointly forecast day-ahead aggregated supply and demand curves for all 24 hours and to embed them in a price-maker storage optimization that quantifies price impact and profitability.

2. Fast Parametric Demand-Curve Forecasting

In this section, we perform a fast prediction of the energy supply and demand curves. This will serve as a baseline model for the rest of this paper. We describe the prediction method applied to demand, noting that the same approach applies to supply. Whenever differences arise, we will specify them. In the results, section 2.3, we will present the model’s performance for forecasting both demand and supply.

In practice, electricity demand as a function of price always exhibits some elasticity Knaut and Paulus (2016), the demand is not fixed for each hour of the day. There is always a minimum demanded quantity, which constitutes the base load that suppliers must provide to their customers, regardless of price. In parallel, through demand response mechanisms or via aggregators, an elastic portion appears. The result is a demand curve $D(p)$ that is not constant.

This curve represents an aggregate of consumer and traditional traders’ demand. The aim of this section is to predict this curve for each delivery hour using machine learning and a method inspired by Ciarreta et al. (2023); Soloviova and Vargiu (2020); Sinha and Lucheroni (2025).

Dataset of interest. In this section, we use a dataset provided by EPEX SPOT consisting of aggregated demand curves from 2018-01-01 to 2024-12-31. We constrain each aggregated curve to lie between -300 EUR and $3\,000$ EUR. This range was chosen to contain every spot price during this period. In practice, on the EPEX SPOT market, -300 EUR represents a lower bound, and $3\,000$ EUR served as the upper bound for day-ahead prices, as shown in Figure 2. This cap remained in place until 2022-04-04, 2022 Commission de Régulation de l’Énergie (CRE) (2022), when France recorded its highest peak price and raised the limit from $3\,000$ EUR to $4\,000$ EUR.

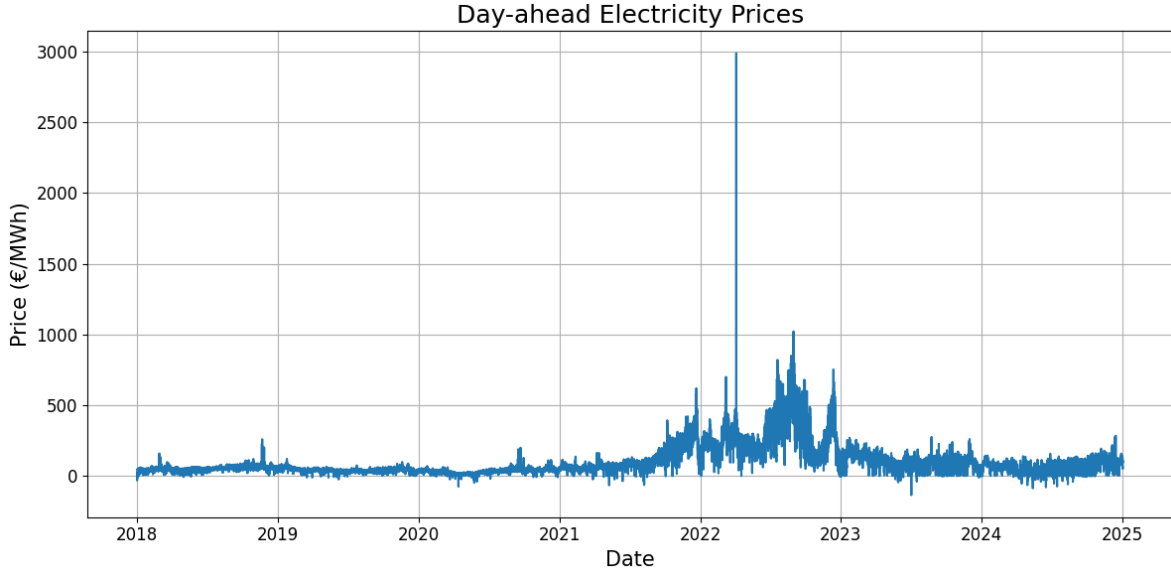


Figure 2: Evolution of the day-ahead electricity price over time between 2018 and 2024

2.1. Problem reduction

One issue with the demand curves across hours is that they are not defined on the same price grid. The most natural approach is to interpolate over the union of all price grids appearing in each curve. Consequently, a machine learning model must predict as many points per hour as the resolution of this union of grids. This leads to a significant increase in the number of points to predict, rendering the task algorithmically very complex.

We reduce the problem to predicting only a few parameters. For this, we begin with the observation that each curve starts with a plateau corresponding to the maximum demand that can be requested, followed by a decreasing elastic segment where arbitrage occurs based on price and the intervention of demand response mechanisms, and ends with a final plateau representing the minimum quantity of energy that will be purchased regardless of price.

This method approximates the curve using a polynomial-based representation. Since the number of points on the aggregated demand curve is not constant, and large gaps may occur between consecutive price levels with nonzero demand, a direct polynomial fit can produce large edge errors. To better capture both the plateaus and the elastic segment, we first linearly interpolate the curve to obtain at least 200 regularly spaced points. This preprocessing step ensures a smoother and more uniform curve, avoiding abrupt jumps between observations.

Our approach, illustrated in Figure 3, has four steps:

1. We detect the first plateau, yielding two parameters U and p_{start} , which are respectively the demand value at this first plateau and the end of this plateau. (Figure 3b)
2. We detect the second plateau, yielding two parameters L and p_{end} , which are respectively the minimum demand required to keep the system running and the end of this plateau. (Figure 3c)
3. Between p_{start} and p_{end} lies the elastic segment; we rescale prices to $[-1, 1]$ and fit a degree-3 polynomial, represented in the Chebyshev basis for numerical stability, resulting in four coefficients $(\text{coef}_0, \dots, \text{coef}_3)$. (Figure 3d)
4. We ensure monotonicity in price by replacing the fitted values with their left-to-right cumulative minima via NumPy's `accumulate` function applied to the minimum function (or maximum for supply prediction). (Figure 3e)

In conclusion, forecasting the demand curve for each hour reduces to predicting eight parameters: $coef_0, coef_1, coef_2, coef_3, U, L, p_{start}, p_{end}$. Alternative specifications for the elastic part, such as higher-degree Chebyshev polynomials (degree 5 or 7), provided similar performance to the degree-3 case, while sigmoid functions were less accurate. Monotone I-splines with four bases and degree 3 yielded results close to the degree-3 polynomial. Since most of the overall forecasting accuracy stems from the correct prediction of the plateaus, which is common to all specifications, we retain the degree-3 Chebyshev approximation as it offers a good compromise between accuracy and simplicity, while remaining computationally efficient in comparison with the other specifications.

The detection of the elastic segment is then performed using Algorithm 1. This procedure consists of listing all discrete slopes between points via finite differences and defining a threshold beyond which the slope is considered large enough to have entered the elastic part of the curve. In our study, we chose a threshold corresponding to the 90% quantile. As soon as a slope exceeds the 90% quantile, we enter the elastic segment, and exit it when the price is bigger than the last point with a slope in this range. On this segment, we fit a polynomial using NumPy’s `Chebyshev` function and enforce monotone non-increase via `np.minimum.accumulate`. Note that this post-processing does not enforce exact continuity at p_{start} and p_{end} ; in practice, any resulting kinks are very small compared to the overall scale. This procedure reduces the number of coefficients that must be estimated but incurs an approximation error shown in Figure 4, with a normalized Mean Absolute Error (nMAE) of about 4 – 5% computed over the whole dataset, from 2018-01-01 to 2024-12-31. The normalization is done over the average value between the two plateaus, meaning that for a given date, if there are $N > 0$ observations, then :

$$\text{nMAE} = \frac{1}{N} \sum_{i=1}^N \frac{|y_i - y_i^{\text{approx}}|}{(U + L)/2} \quad (1)$$

with U, L the plateaus, y the real data point and y^{approx} the approximated ones.

Algorithm 1

Require: Sorted arrays x, y ; percentile pct

Ensure: p_{start}, p_{end} where $|\Delta y / \Delta x|$ exceeds the pct percentile

- 1: Compute slope $\leftarrow \text{gradient}(y, x)$
- 2: Compute threshold $thr \leftarrow \text{percentile}(|\text{slope}|, pct)$ corresponding to the quantile of level pct
- 3: Find indices $idx \leftarrow \{ i \mid |\text{slope}_i| > thr \}$
- 4: **if** idx is empty **then**
- 5: **return** x_{\min}, x_{\max}
- 6: **else**
- 7: **return** $x[idx_0], x[idx_{\text{last}}]$
- 8: **end if**

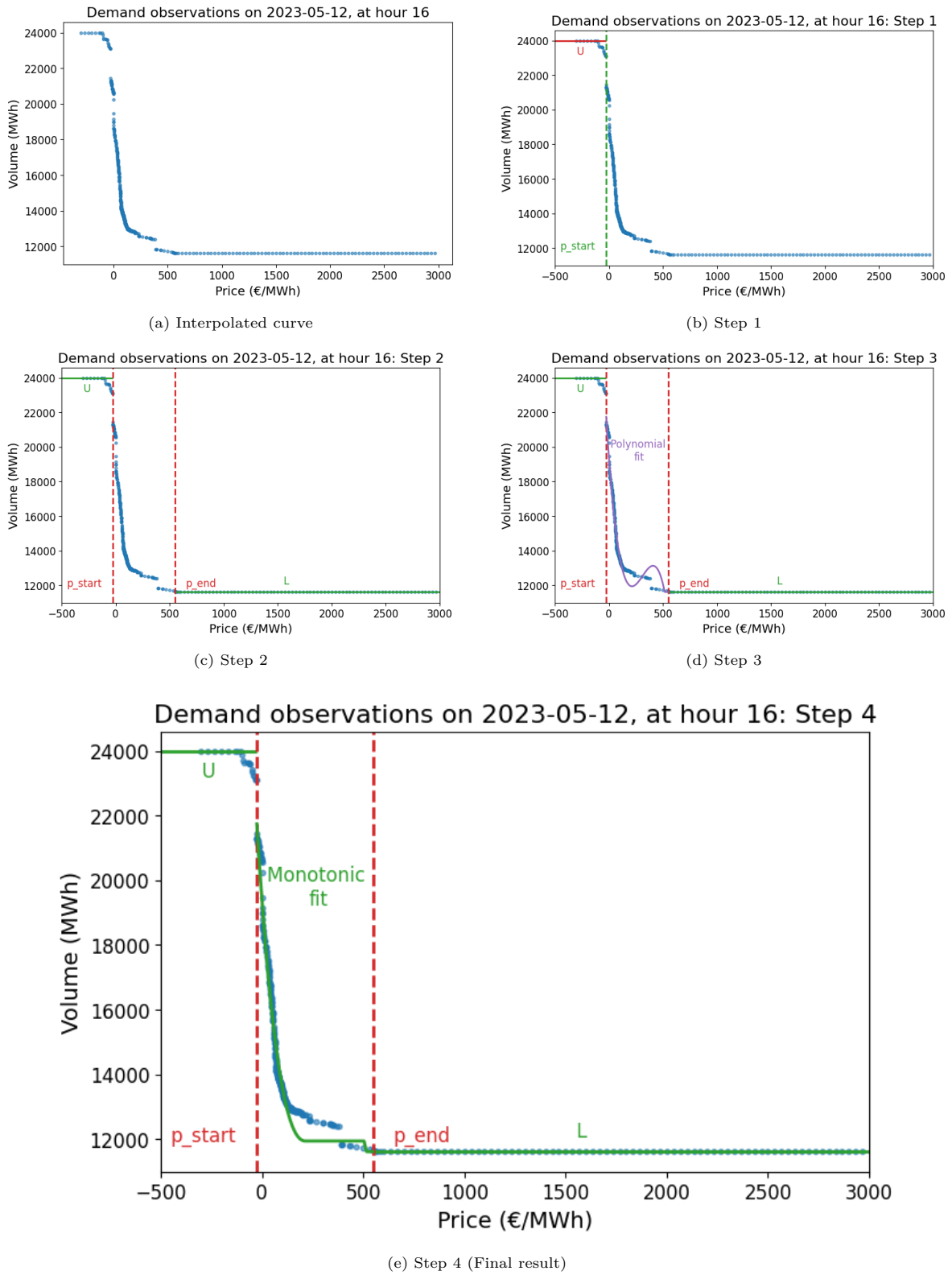


Figure 3: Progressive approximation steps: from interpolation to the final reconstruction.

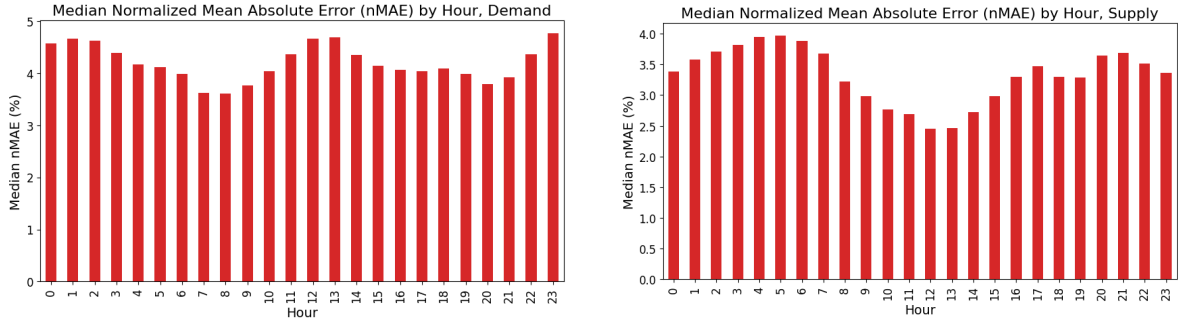


Figure 4: Median value for every hour of the normalized Mean Absolute Error between the original points and the polynomial approximation for the demand (left) and the supply (right) curves.

2.2. Choice of features

A key aspect in machine learning models is feature selection. For this demand-prediction problem, three types of features are used. Here, each curve is characterized by eight parameters, which we naturally treat as a time series available up to the day before prediction.

Time series. The first feature category consists of elements derived from these time series. For each parameter, we include its lag values from one day ago up to 14 days prior, in order to capture immediate trends. Because errors in plateau values can produce large overall forecast errors (potentially shifting the entire curve), we add some specific features to predict U and L . Specifically, we incorporate the 24 hourly U and L values from the previous day.

Features from the original points. The second feature type captures properties of the pre-reduction curves, the point clouds defined by couples (Volume, Price). From each cloud, we compute the skewness, and kurtosis. We also compute the volume of the largest single order placed, the number of orders submitted before p_{start} , the number submitted after p_{end} , and the total order count. All those features are shifted by 24 hours.

External features. The final feature category consists of external factors. These are the following :

- Categorical variables indicating the hour, whether a date falls on a public holiday, during the winter school holidays, at night, within peak hours, on a weekend, or during a specific event (e.g., a concert or the Olympics).
- Day-ahead forecast of electricity demand based on European Network of Transmission System Operators for Electricity (ENTSO-E) predictions.⁴
- Temperature, solar irradiance, average wind speed, and relative humidity for major French cities (Bordeaux, Toulouse, Marseille, Paris, Lille).⁵⁶
- The previous day's day-ahead electricity price.⁷

For each external data series, we applied a preprocessing step to handle daylight-saving time shifts: when an hour was missing due to the switch to summer time, we added it by duplicating the subsequent theoretical hour; when there was an extra hour due to the switch back to winter time, we removed the

⁴Source: <https://transparency.entsoe.eu/>

⁵Source: Copernicus ERA5. These data are used here as a consistent and publicly available proxy. In practice, a trader would rely on operational weather forecasts available in real time.

⁶To predict the supply curves, we additionally include wind speed and humidity.

⁷Source: EPEX SPOT

second occurrence. To justify the inclusion of external data, Figure 5 shows the Spearman correlation between each external feature and the coefficients we aim to predict. These correlations are computed on the first differences of each series to remove common trends. With over 50 000 observations, even small rank correlations are statistically detectable (test statistics scale as \sqrt{n} , with n the number of observations); we therefore retain features with $|\rho| \geq 0.05$.

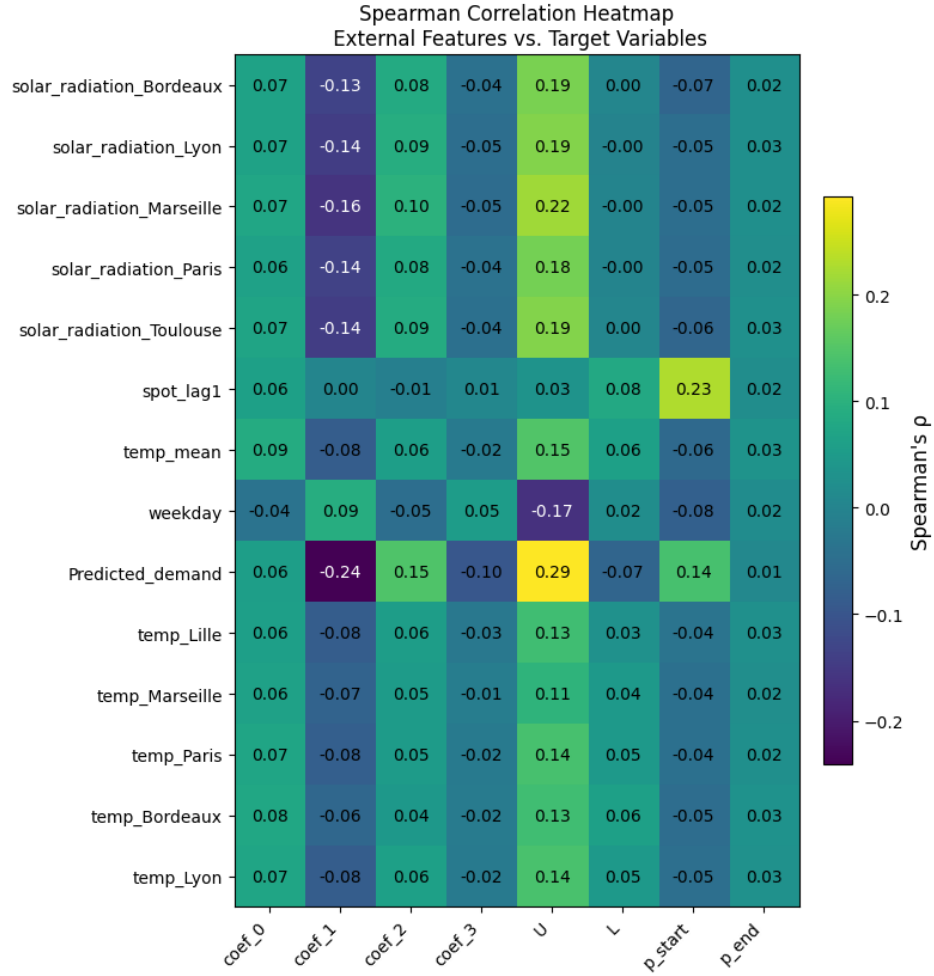


Figure 5: Spearman's correlation heatmap between the aimed coefficients and the external features for the demand forecast.

2.3. Model and results

Using the features defined in section 2.2, we use Extreme Gradient Boosting (XGBoost). XGBoost is a supervised learning method of the gradient boosting type based on building a series of decision trees that minimize a loss function. For further details on XGBoost, we refer the reader to the seminal work of Chen and Guestrin Chen and Guestrin (2016). We train eight separate models, one for each parameter, using the `quantileerror` loss, which is the standard quantile loss that penalizes predictions asymmetrically to target a given conditional quantile. Predictions are done one hour at a time. The fast execution of the model makes it possible to perform an exhaustive search of the hyperparameters. The selected ones are described in Table 1 (for the supply prediction, they are described in Table 2). All training is performed on 85% of the dataset, covering early 2018 to late 2023. The remaining year 2024 is used to test the model.

Table 1: Chosen hyperparameters for each target (XGBoost) for the demand forecast

Target	quantile_alpha	learning_rate	max_depth	min_child_weight	subsample	colsample_bytree	reg_lambda	reg_alpha	gamma
coef_0	0.5	0.030	3	3	0.6	1.0	1	1.0	0.3
coef_1	0.5	0.005	3	7	0.4	0.8	10	1.0	0.5
coef_2	0.5	0.030	5	5	0.6	0.6	10	1.0	0.3
coef_3	0.5	0.010	3	1	0.7	0.8	1	0.0	0.0
U	0.5	0.030	5	1	0.7	1.0	1	0.0	0.0
L	0.8	0.030	5	1	0.7	1.0	1	0.0	0.0
p_start	0.4	0.010	3	1	0.7	0.8	1	0.0	0.0
p_end	0.5	0.010	3	1	0.7	0.8	1	0.0	0.0

Table 2: Chosen hyperparameters for each target (XGBoost) for the supply forecast

Target	quantile_alpha	learning_rate	max_depth	min_child_weight	subsample	colsample_bytree	reg_lambda	reg_alpha	gamma
coef_0_supp	0.7	0.03	3	6	0.6	1.0	0.5	0.8	0.0
coef_1_supp	0.5	0.01	3	8	0.5	0.8	8.7	0.8	0.9
coef_2_supp	0.3	0.02	6	15	0.5	0.6	15.1	1.3	0.4
coef_3_supp	0.7	0.01	5	2	0.7	0.7	1.3	0.0	0.0
U_supp	0.5	0.05	3	2	0.5	1.0	1.5	0.0	0.5
L_supp	0.5	0.04	3	6	0.8	1.0	1.0	0.0	0.0
p_end_supp	0.5	0.01	5	10	0.5	0.7	0.4	0.0	0.2
p_start_supp	0.7	0.01	2	6	0.6	0.7	1.4	0.0	0.0

The results are evaluated in two steps. First, we directly compare the prediction with the polynomial approximation; then, we compare it with the actual bid curve data points. These comparisons are always performed after reconstruction of the curve with the parameters.

Figure 6 shows the boxplots and the distributions of the nMAEs for both demand and supply. The distributions are smoothed using Kernel Density Estimation (KDE) with a Gaussian kernel. For the demand curves, the model achieves a median error of 7.2% on the full grid and 7.5% on the elastic part, while for the supply curves the median error is 10.7% on the full grid and 11% on the elastic part. To compute this error, we discretize the state space into 2000 points and calculate the MAE over both the full grid and solely within the elastic region to reduce the influence of the upper and lower plateaus. Finally, we normalize each error as described in (1) with the true values of U and L .

However, since electricity price dynamics are heavily influenced by whether an hour is peak or off-peak (peak hours involve more market participants), Figure 7 shows the hourly MAE between the predicted curve and the true polynomial approximation and we compute in Figure 8 the median of all nMAEs for each hour. The results are similar whether the error is applied only to the elastic part or to the entire curve, with a median nMAE ranging from 6.31% at best to 9.17% at worst for the demand curves and from 9.5% to 12% for the supply curves. The normalized error shows little dependence on the hour of the day.

Another comparison to assess prediction quality is to compare the MAE of our model's prediction with that of a naive predictor, which uses the coefficients from the same hour on the previous day. The quotient of both values is the Mean Absolute Scaled Error (MASE) and in Figure 9 we see that our model clearly outperforms the naive one.

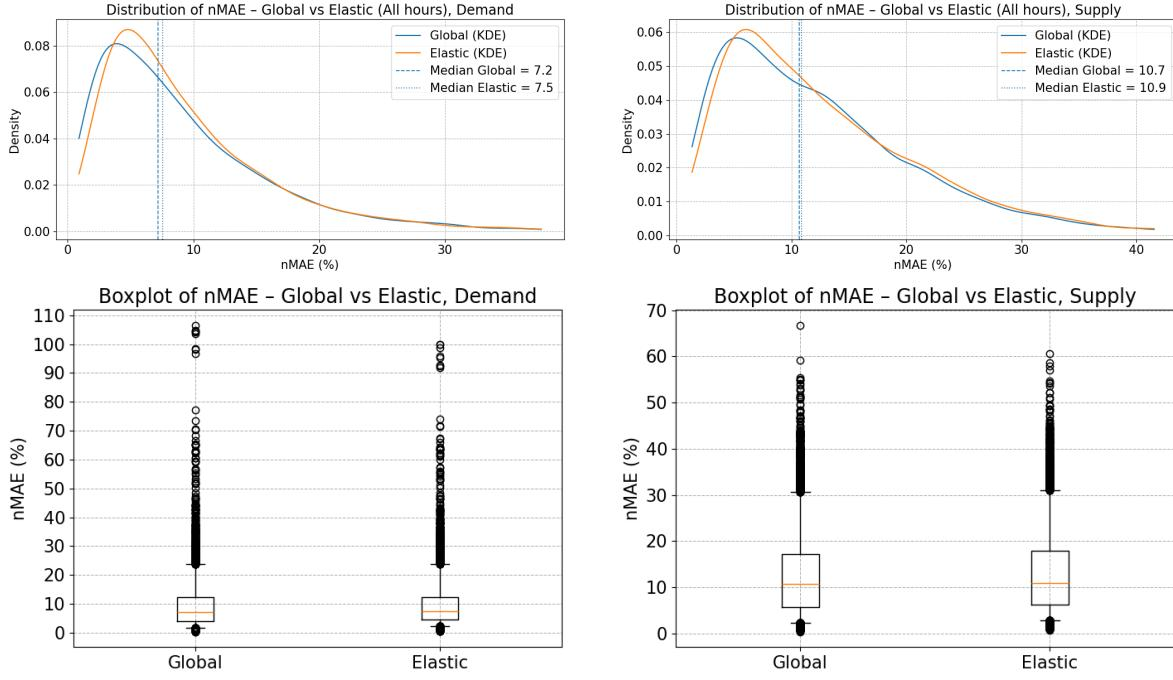


Figure 6: Distributions and boxplots of the nMAE between the predicted approximation of the curve and the true polynomial approximation. Demand results are shown on the left, and supply results on the right.

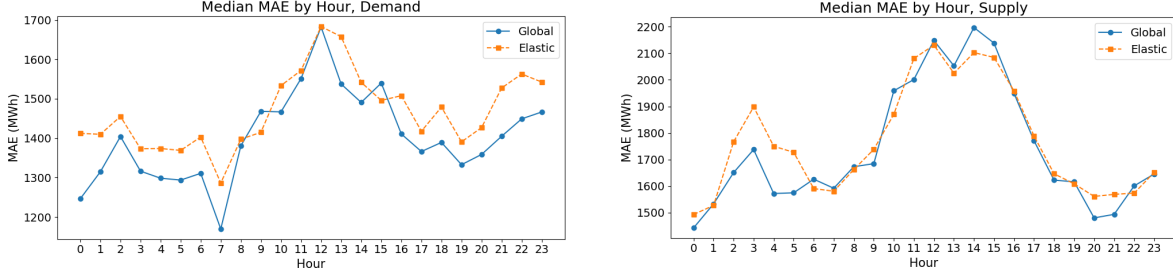


Figure 7: Median MAE between the predicted approximation of the curve and the true polynomial approximation, for every hour. Demand results are shown on the left, and supply results on the right.

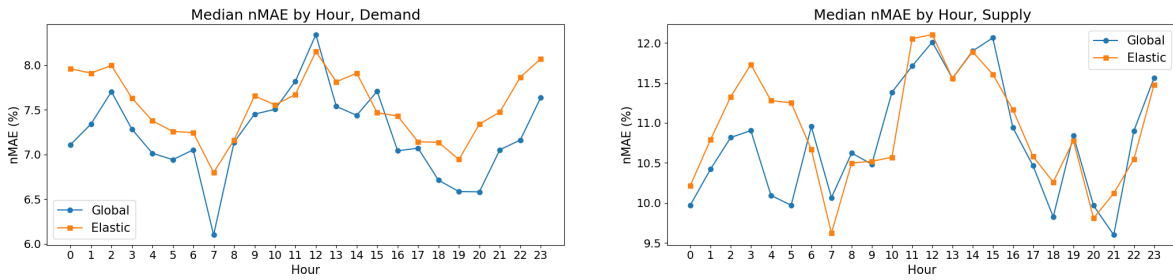


Figure 8: Median nMAE between the predicted approximation of the curve and the true polynomial approximation, for every hour. Demand results are shown on the left, and supply results on the right.

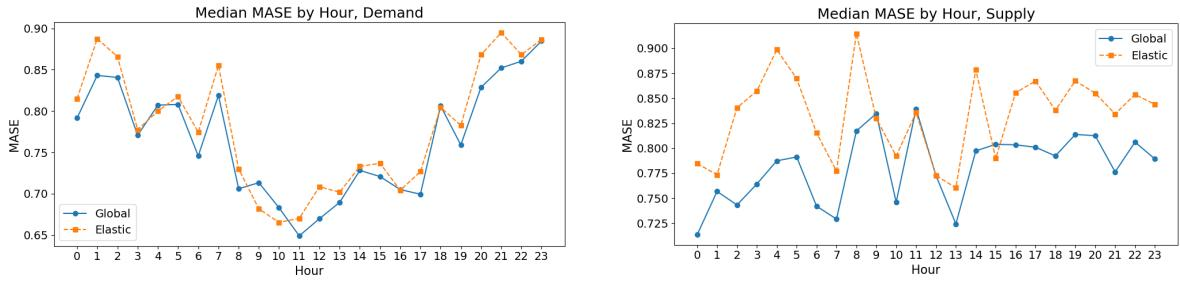


Figure 9: Median MASE between the predicted approximation of the curve and the naive prediction, for every hour. The error on the whole curve is on the left. Demand results are shown on the left, and supply results on the right.

The model succeeds at its primary goal (predicting curves via polynomial approximation), but it's also useful to compare these estimates against the actual data points. Figure 10 shows the distribution and box-plot of the nMAEs across the test dataset. For the demand curves, it performs with a median of 9.71%, a 5th percentile of 3.28%, and a 95th percentile of 25.4%. For the supply curves, it performs with a median of 9.99%, a 5th percentile of 3.34%, and a 95th percentile of 27.86%. As before, the error remains uniform across all hours, as illustrated in Figure 11 hourly error plot. We compute the MASE in Figure 12 and we see that our model again outperforms the naive one for almost every hour. We provide examples of prediction in Figure 13 for both supply and demand.

One of XGBoost's key strengths is its speed. Our aim in this section was to build a tool that is both effective and practical: by reducing the problem's dimensionality, an operator can generate all daily predictions before submitting market orders. In our case, training on five years of historical data (2018-2023) to estimate all eight coefficients takes 1 minute on commodity hardware ⁸ and the prediction of an hour takes less than 0.5 second, making it suitable for real-time applications with minimal infrastructure cost. This approach is not only fast and accurate but also scalable: the architecture allows to enrich the feature set or replace the polynomial basis (e.g., with monotone splines) without prohibitive computational overhead.

⁸Performed on a computer with a CPU AMD Ryzen 7 5800X3D and a GPU Nvidia RTX 3070.

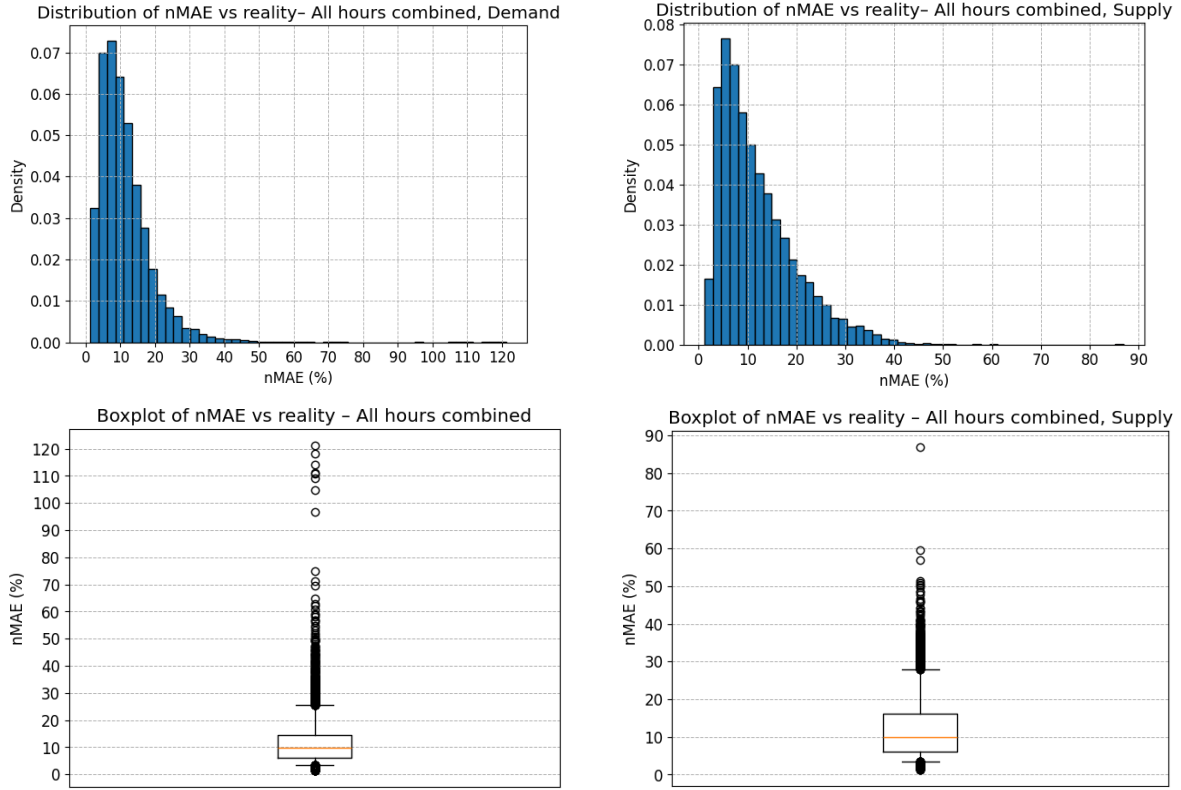


Figure 10: Distribution and boxplots of the nMAE between the predicted approximation of the curve and real points. Demand results are shown on the left, and supply results on the right.

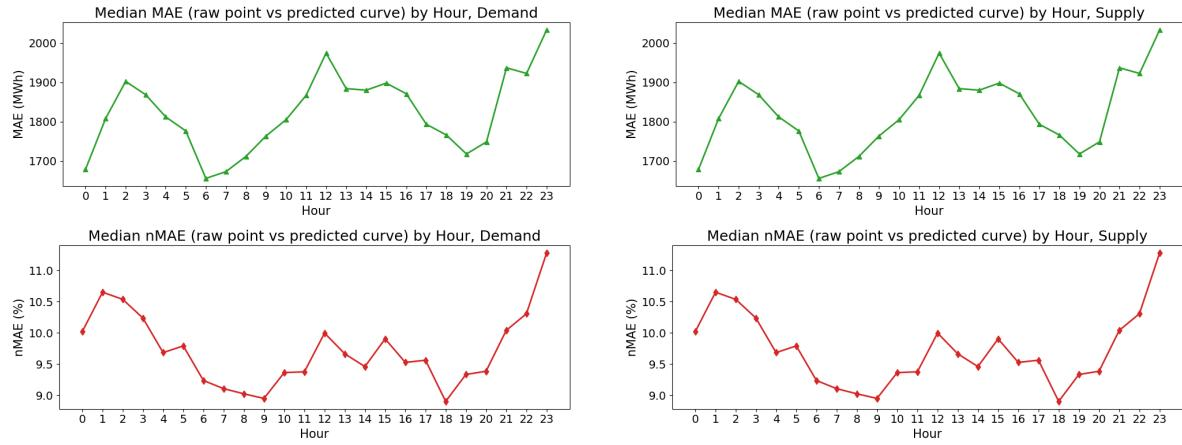


Figure 11: Median MAE (left) and nMAE (right) between the predicted approximation of the curve and the true curve, for every hour.

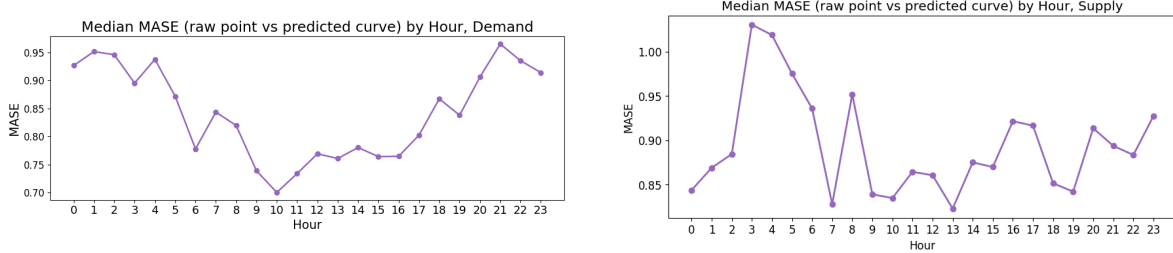


Figure 12: Median MASE between the predicted approximation of the curve and the true curve, for every hour. Demand results are shown on the left, and supply results on the right.

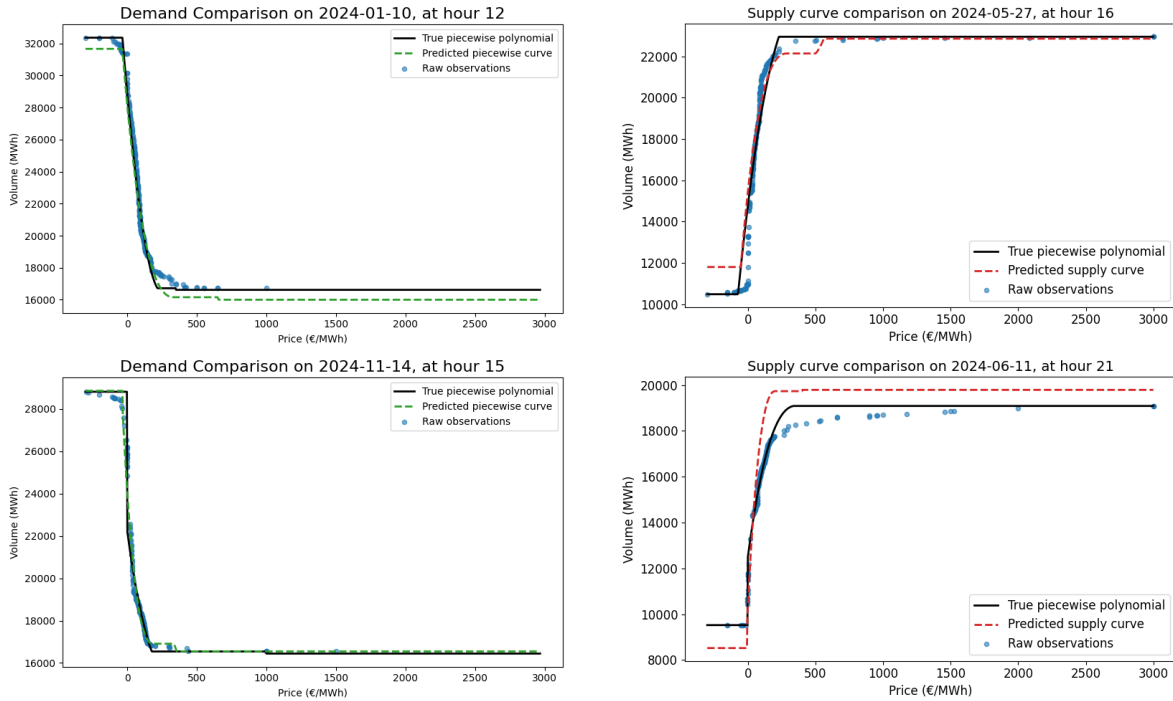


Figure 13: Example of predictions compared to the actual data point and the polynomial approximation. Demand results are shown on the left, and supply results on the right.

In this section, we have therefore developed a prediction method with several concrete advantages. The first advantage is speed: since each curve is summarized by eight parameters, both training and inference are very fast, making deployment at $J - 1$ straightforward for an industrial user. The second advantage is interpretability: the decomposition allows each coefficient to be directly understood (for instance for the demand curves, if U increases, one can diagnose an increase in the system's energy absorption capacity).

This model is effective when the regime behaves normally, but its deterministic nature prevents it from accurately capturing more extreme regimes, where the curve's shape could deviate due to exceptional situations. A further limitation is that our model does not provide any information about the underlying order structure that generates each curve. It is thus an efficient day-to-day tool but lacks depth for more detailed analysis. The goal of the next section is to introduce a second model, slower and less suitable for $J - 1$ deployment, but able to address these limitations. We will then compare with the baseline model developed in the current section.

3. Generative Supply Curves from Marked Point Processes and DDPMs

In this section, we develop a generative prediction of day-ahead supply and demand curves by explicitly modelling the order-level structure from which they are built. Whereas the previous section modelled full curves directly, here we treat each submitted order as an individual object. Their distribution is learned by a generative model, which produces synthetic orders that are then aggregated to reconstruct the curves. This approach captures how order prices and volumes depend on factors such as weather variables and fuel prices. In contrast to the fast model, it yields probabilistic forecasts rather than single deterministic curve realizations. We describe the modelling approach on the supply side, but implement it and report results for both demand and supply.

3.1. The supply curve modeling

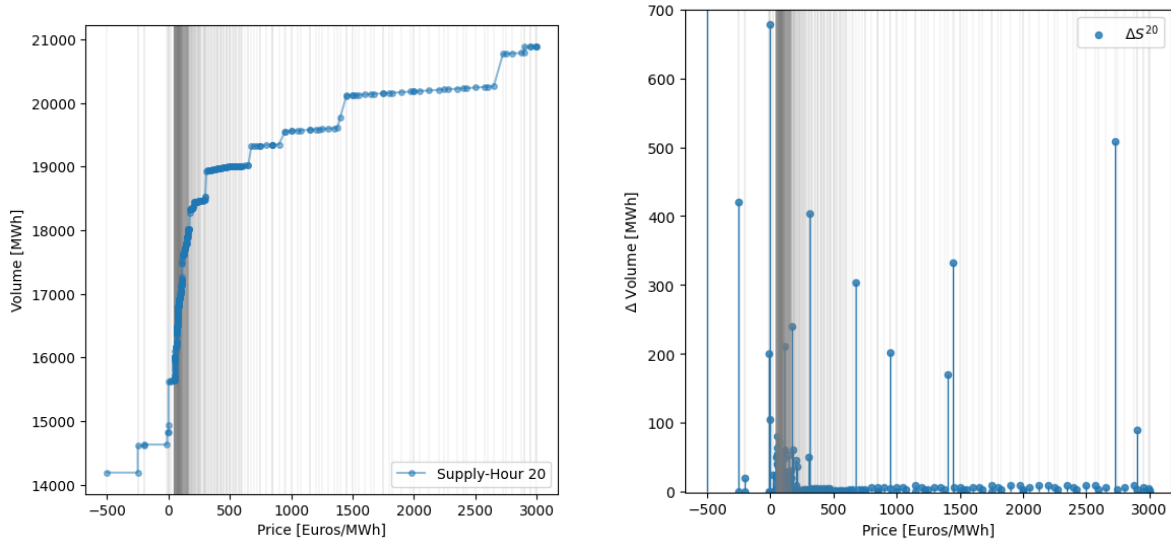


Figure 14: Supply curve and marked point process $(P_n^{20}, \Delta S_n^{20})_{n=1}^{408}$ for hour 20 on 2020-10-05

We interpret the supply curve as a set of arrival prices paired with offered volumes over the 24 hours, modeled as a marked Cox process (a doubly stochastic Poisson process with marks; see, e.g., Jacobsen (2006)). For a given hour $h \in 1, \dots, 24$, let $(P_n^h, S_n^h)_{n=0}^{N^h}$ denote the price–volume points defining the supply curve, shown in Figure 14. Here, $P_0^h = -500$, $P_{N^h}^h = 3000$, the prices $(P_n^h)_{n=0}^{N^h}$ are strictly increasing, and S_n^h is non-decreasing. We compute volume increments across the curve:

$$\Delta S_n^h = S_n^h - S_{n-1}^h, \quad n = 1, \dots, N^h, \quad (2)$$

and consider $(P_n^h, \Delta S_n^h)_{n=1}^{N^h}$, displayed in Figure 14. To model all 24 hours jointly, we take every distinct price value that appears in any hourly curve, and collect these values into a single list

$$\cup_{h=1}^{24} \{P_n^h : n = 1, \dots, N^h\},$$

from which we construct an increasing ordered sequence

$$(P_m)_{m=1}^M.$$

This sequence provides a unified price grid at the day level and offers a common support on which all hourly curves can be aligned. For each P_m , we attach the 24-volume vector (mark)

$$\Delta S_m := (\Delta S_m^1, \dots, \Delta S_m^{24}), \quad \Delta S_m^h := \begin{cases} \Delta S_n^h, & \text{if } P_m = P_n^h \text{ for some } n \in \{1, \dots, N^h\}, \\ 0, & \text{otherwise.} \end{cases} \quad (3)$$

The encoding $(P_m, \Delta S_m)_{m=1}^M$ captures complex supply offers such as block orders (all-or-nothing bid spanning consecutive hours at one price, yielding multiple nonzero entries in ΔS_m) and flexible hourly block orders (one-hour blocks placed over an admissible hour set). Figure 15 illustrates this encoding, computed via (3).

We assume that $(P_m, \Delta S_m)_{m=1}^M$ is a realization of a marked Cox process $(\mathbf{P}, \Delta \mathbf{S})$: the arrivals \mathbf{P} follow a Cox process with stochastic intensity λ , which is a random variable conditioned on exogenous random features \mathbf{X}^P . The volume marks $\Delta \mathbf{S}$ are 24-dimensional and modelled as random variables conditional on price \mathbf{P} , and additional features \mathbf{X}^S . The feature set includes weather and fuel price variables. The generative framework allows for this dependences through latent variables \mathbf{Z}' and \mathbf{Z} , obtaining

$$\lambda \sim \mathcal{L}(\mathbf{Z}' \mid \mathbf{X}^P), \quad \Delta \mathbf{S} \sim \mathcal{L}(\mathbf{Z} \mid \mathbf{P}, \mathbf{X}^S). \quad (4)$$

For instance, setting $\mathbf{X}^P, \mathbf{X}^S = \mathbf{T}^{\text{mean}}$, where \mathbf{T}^{mean} is the mean temperature, would encode dependence on price and mean temperature only. We do not expect to capture other complex supply offers such as linked block orders (child blocks acceptance based on a revenue threshold across hours), nor minimum income condition orders; these create recursive, cross-mark constraints that are outside our present scope.

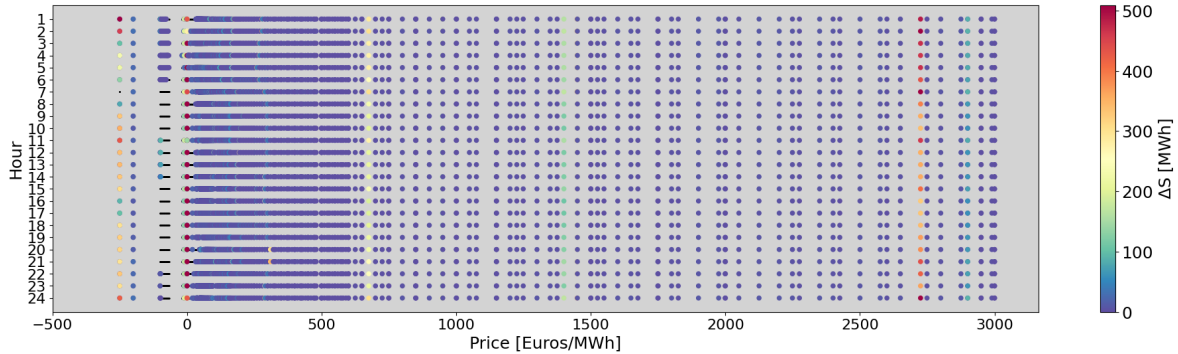


Figure 15: $(P_m, \Delta S_m)_{m=1}^{975}$ on 2020-10-05. Black dots represent the 0-values introduced on ΔS in equation (3).

For the generative task, we use DDPM (Ho et al. (2020); Song et al. (2021)), a class of deep generative models that learn to reverse a gradual noise corruption process applied to data, allowing to generate new samples by starting from pure noise and iteratively recovering realistic data. We generate supply curves using DDPM in two stages:

1. Stage 1: We generate λ conditional on the exogenous features \mathbf{X}^P , used as labels on the DDPM. The resulting sample is denoted by $\tilde{\lambda}$, which we use to draw the arrival prices \mathbf{P} by thinning (Lewis and Shedler (1979)). The price sample obtained in this step is denoted by $(\tilde{P}_m)_{m=1}^M$.
2. Stage 2: We generate the volume marks $\Delta \mathbf{S}$ conditional on the sample $(\tilde{P}_m)_{m=1}^M$ and on the exogenous features \mathbf{X}^S , also used as labels on the DDPM. The resulting sample is denoted by $(\Delta \tilde{S}_m)_{m=1}^M$.

We then reconstruct cumulative volumes via

$$\tilde{S}_m = \Delta \tilde{S}_m + \tilde{S}_{m-1}, \quad m = 1, \dots, M, \quad (5)$$

so that $(\tilde{P}_m, \tilde{S}_m)_{m=0}^M$ determines the generated supply curves. Figure 16 illustrates these stages. The training and generation procedures for each stage are detailed in Sections 3.1.1 and 3.1.2 below.

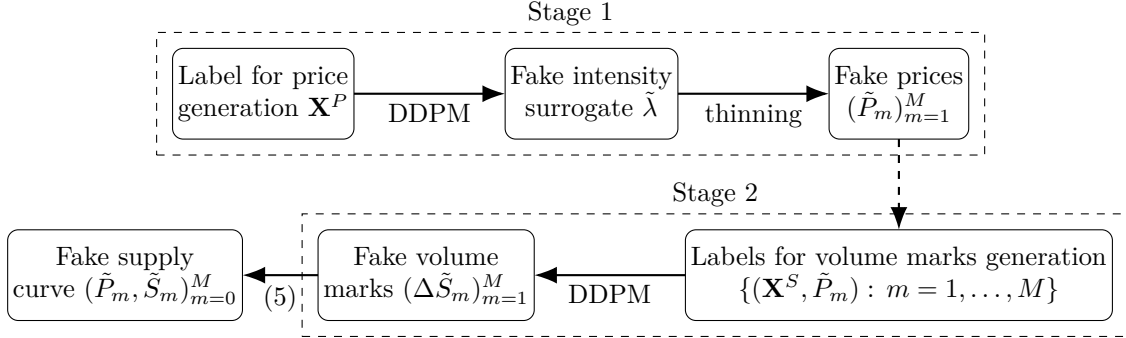


Figure 16: Stages in the generation of supply curves

To keep focus on price-dependent order-level modelling, in (5), we take \tilde{S}_0 from data: $\tilde{S}_0 = (S_0^1, \dots, S_0^{24})$, since it always corresponds to the same price level of -500 EUR. This simplifies the evaluation but reduces generalizability, since the initial offer does not adapt to market conditions. A natural extension is to describe \tilde{S}_0 using the first plateau values of the fast parametric model from Section 2, which yields more accurate results than alternative stochastic parametrizations—such as fitting an Ornstein–Uhlenbeck process to historical data—or by learning it through an additional generative model.

The DDPM in both stages is designed to generate samples of a random variable \mathbf{X} conditioned on a specified label $\mathbf{X}^{\text{label}}$. The training process, illustrated in Figure 17, proceeds as follows. At each time step, the model receives a noised version of the data \mathbf{X}' (the original data \mathbf{X} perturbed with Gaussian noise \mathbf{Z}) together with the label $\mathbf{X}^{\text{label}}$, and learns to predict $\hat{\mathbf{Z}}$, the noise that was originally added. After training, Algorithm 2 generates samples by running the process in reverse: starting from pure noise \mathbf{X}' , the model iteratively removes noise using the predicted $\hat{\mathbf{Z}}$, and after several reverse steps recovers a sample \mathbf{X} that follows the data distribution. Because noise prediction is conditioned on $\mathbf{X}^{\text{label}}$, the sampling procedure in Algorithm 2 generates samples of \mathbf{X} associated with the label $\mathbf{X}^{\text{label}}$. In the following sections, we describe each stage of this procedure in detail, focusing separately on price arrivals and volume marks.

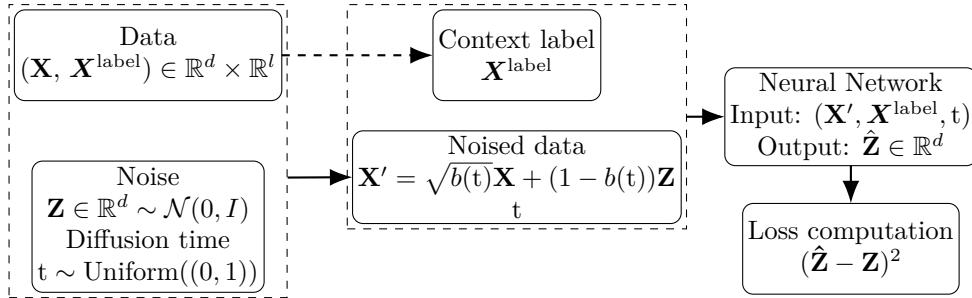


Figure 17: DDPM noise prediction with labels

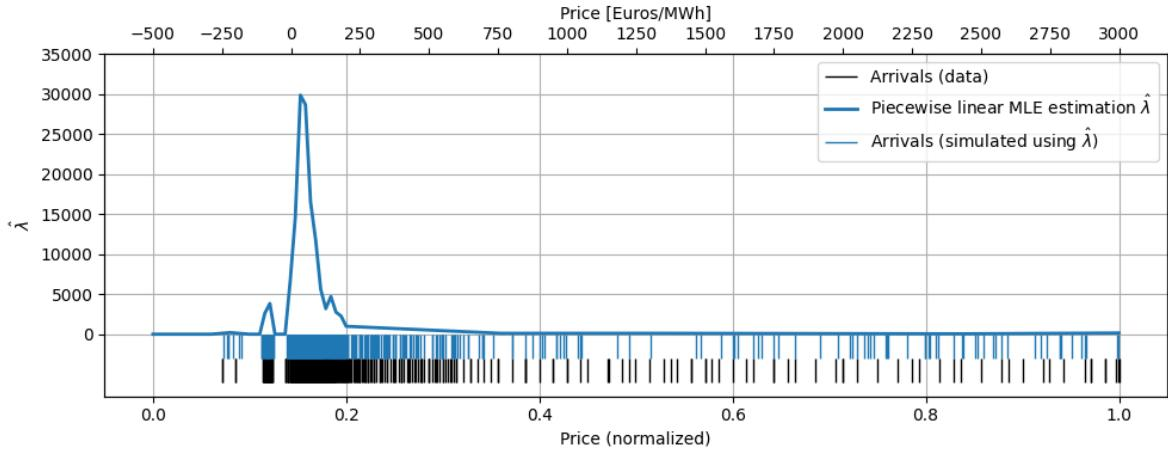
Algorithm 2 DDPM sampling with labels

Require: Array $\mathbf{X}^{\text{label}} \in \mathbb{R}^l$, denoising steps K , $t \mapsto \beta(t)$, $\alpha \in \mathbb{R}$

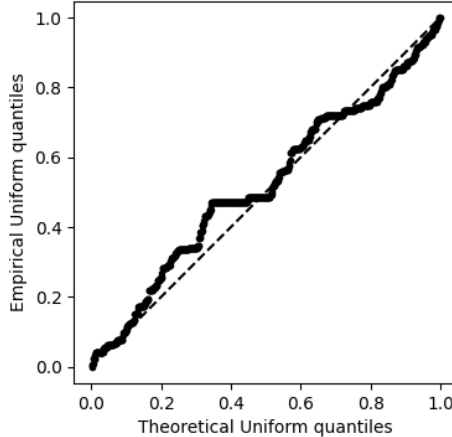
- 1: $b = \text{CUMPROD}(1 - \beta)$
- 2: Sample $\mathbf{X}' \in \mathbb{R}^d \sim \mathcal{N}(0, I)$,
- 3: **for** $k = 1$ **to** K **do**
- 4: $t = k/K$
- 5: $(\mathbf{X}', \mathbf{X}^{\text{label}}, t) \mapsto \hat{\mathbf{Z}}$ using DDPM
- 6: $\mathbf{X}' = (1 - \beta(t))^{-1/2}(\mathbf{X}' - \beta(t)(1 - b(t))^{-1/2}\hat{\mathbf{Z}})$
- 7: Sample $\mathbf{Z}' \in \mathbb{R}^d$
- 8: $\mathbf{X}' = \mathbf{X}' + \sqrt{\alpha\beta(t)}\mathbf{Z}'$
- 9: **end for**

3.1.1. Arrival price process generation

We normalize prices from $(-500, 3000]$ to $(0, 1]$, and by an abuse of notation, we still denote the normalization by \mathbf{P} . To numerically represent $\boldsymbol{\lambda}$, we select a 30-point grid on $(0, 1]$. The grid is coarse on the intervals $(0, 0.1)$ and $(0.3, 1]$ with 5 equally spaced points each, corresponding to the price ranges $[-500, -150]$ and $[550, 3500]$, respectively. On the interval $[0.1, 0.3]$, where day-ahead price values concentrate, we select the remaining 20 equally spaced points. The number of grid points on each subinterval was tested extensively with multiple configurations, and the chosen allocation provides a suitable balance: it preserves the overall shape of the fitted curves while maintaining a low computational cost. Using the price arrivals $(P_m)_{m=1}^M$ for a given day, we estimate a piecewise-linear $\hat{\lambda}$ by maximum-likelihood estimation (MLE), and treat $\hat{\lambda}$ as a surrogate realization of $\boldsymbol{\lambda}$. Numerical tests revealed that polynomial and Gaussian-kernel parametrizations are unstable for DDPM training; however, piecewise-linear surrogates proved to be robust. Figure 18a displays the real price arrivals (data), the parametrization $\hat{\lambda}$ obtained by MLE from these arrivals, and a sample of arrivals generated from $\hat{\lambda}$ by standard thinning. To assess the fit, we apply the time-rescaling theorem: given the fitted piecewise linear surrogate $\hat{\lambda}$, we compute the compensator at observed arrival times. The intercompensator gaps should be i.i.d. $\text{Exp}(1)$; applying the exponential cumulative function to these gaps yields values that should be uniformly distributed on $[0, 1]$. Figure 18b shows the resulting quantile-quantile plot.



(a) Arrivals (data), surrogate $\hat{\lambda}$ and generated arrivals



(b) Q–Q plot of transformed interarrival times under $\hat{\lambda}$ vs. $U[0, 1]$ distribution.

Figure 18: MLE estimation of surrogate $\hat{\lambda}$ on 2020-10-05

The DDPM then learns the $\mathcal{L}(\mathbf{Z}' \mid \mathbf{X}^P)$ in (4), where \mathbf{X}^P is the 12-dimensional feature vector comprising fuel prices and weather variables. These include Coal, Oil, and Gas prices, as well as the minimum, maximum, and mean values of Air Temperature (AT), Global Horizontal Irradiance (GHI), and Wind Speed (WS). The corresponding summary statistics are reported in Table 3. Fuel price variables are computed as described in Section Appendix A of the Appendix. We use country-level weather variables for France from the Copernicus ERA5 dataset (see External features in Section 2.2), whose values are provided as post-processed area-weighted spatial averages of the underlying gridded fields. To avoid the 2021–2022 volatility regime shift in fuel prices and to reduce training costs, we restrict the dataset to the period 2017-10-23 to 2020-12-31.

Using the EPEX SPOT data, we compute 1166 surrogates $\hat{\lambda}$ (one per day from 2017-10-23 to 2020-12-31) for the supply side, obtaining 1166 data points in dimension 42 (the first 30 entries corresponding to the piecewise-linear parametrization $\hat{\lambda}$ and 12 entries to the features of Table 3). We select the following parameters for Algorithm 2, which we maintain throughout the following sections. The diffusion steps are $K = 501$, the noise schedule β is defined through linearly increasing variance coefficients, starting from a small value $\beta_1 = 10^{-4}$ up to $\beta_2 = 0.02$. The parameter α used in generation is set to $1/3$. We train the model for 2×10^4 epochs with a batch size of 256. Training time was 20

	Coal	Oil	Gas	AT mean	AT min	AT max	GHI mean	GHI max	WS mean	WS min	WS max
	[EUR/MWh]	[EUR/MWh]	[EUR/MWh]	[°C]	[°C]	[°C]	[W/m ²]	[W/m ²]	[km/h]	[km/h]	[km/h]
Min	34.09	28.35	17.80	267.82	264.54	271.23	14.36	68.18	1.40	0.97	1.76
Max	63.34	129.20	80.97	301.55	294.39	308.75	345.70	906.10	7.65	6.14	9.00
Mean	47.11	92.77	46.93	285.10	281.30	289.12	149.44	478.01	3.21	2.48	3.95

Table 3: Summary statistics of features for λ generation. The data cover the period from 2017-10-23 to 2020-12-31. Since the minimum of GHI is always 0.00, it is not reported.

minutes⁹.

Figure 19 compares the real surrogate $\hat{\lambda}$ of Figure 18a with one generated (fake) sample $\tilde{\lambda}$, and displays further samples of arrival prices. We use the same modelling and training parameters for the demand side, yielding similar results.

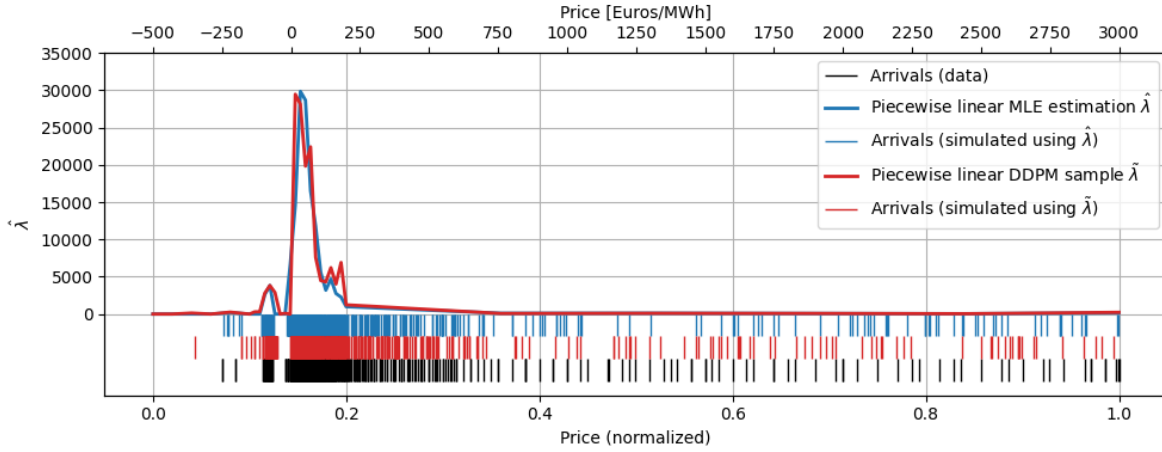


Figure 19: Arrivals (data), surrogates, and generated arrivals on 2020-10-05

3.1.2. Marks volumes generation

In this section, following (4), we use the samples $(\tilde{P}_m)_{m=1}^M$ obtained with the model of Section 3.1.1 as inputs to generate samples of ΔS . Figure 20 shows that ΔS values cluster around specific price–volume points, reflecting the nominal generation capacities of production assets and allowing the likely producer type to be inferred from offer size and price. The figure also highlights a clear distinction between small and large offers, which motivates the use of two separate DDPMs for generating ΔS : one for values above 200 MWh and another for values below this threshold. The choice of 200 MWh was not arbitrary; several threshold values, both lower and higher, were tested numerically, and 200 MWh consistently provided the best empirical performance in terms of model stability and fidelity of the observed distribution.

A particular challenge arises from the zeros that were introduced during the data transformation in (3). In the empirical distribution, these zeros correspond to a heavy point mass (Dirac mass) at zero. However, DDPMs and more generally diffusion-based generative models are designed to approximate continuous probability densities and rely on the forward noising process and score estimation being applied to data with a non-singular, smooth density. A Dirac mass violates these assumptions because it introduces an infinite spike in the density that cannot be diffused appropriately or learned by the model.

To circumvent this incompatibility, we replace zeros with samples from small-variance Gaussian

⁹Performed on Google Colab on a machine with an Intel Xeon CPU at 2.20GHz, 2 cores, and 12 GB of RAM.

distributions centred slightly below zero. For the low-volume model, we use $\mathcal{N}(-50, 5)$, and for the high-volume model, $\mathcal{N}(-250, 25)$. These distributions were selected after repeated trials to ensure that the artificially introduced values remain clearly separated from the genuine ΔS distribution while also maintaining approximate symmetry around zero. This treatment removes the Dirac mass, rendering the transformed data suitable for DDPM training. For the demand side, we apply the same procedure with a threshold of 450 MWh and use $\mathcal{N}(50, 5)$ and $\mathcal{N}(250, 25)$ for the corresponding low-volume and high-volume models.

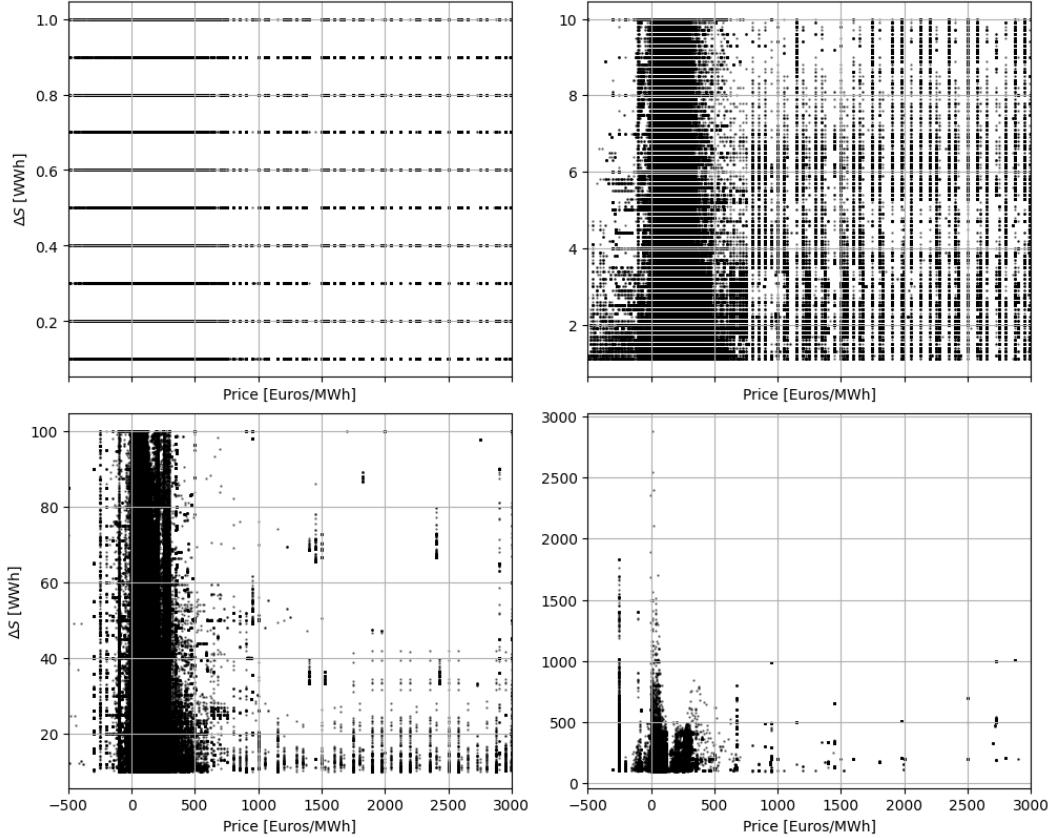


Figure 20: ΔS against arrival prices in 2020. The range of ΔS is divided into four intervals across the figures.

To justify the selection of features, Figure 21 displays the relationship between price, offered volumes, and exogenous variables, such as weather conditions and fuel prices. Patterns indicate that the type of producer, whether renewable or conventional, plays a central role in shaping bidding strategies. For instance, the lack of sensitivity of specific volume values to solar irradiance suggests solar producers do not bid at such volume levels. Similarly, insensitivity to fuel prices helps identify volume ranges for which bids from conventional producers are unlikely to be submitted. Although such observations may appear straightforward from a production perspective, we highlight that EPEX data is anonymous, preventing direct identification of producers or technologies behind specific offers. In a full-information setting, where producer identities were available, supply curve generation strategies would be refined considerably. Nevertheless, as we will demonstrate, even when trained on anonymous data, the DDPM model is still able to capture meaningful dependencies between bid sizes and prices on weather and fuel price variables.

Beyond these qualitative observations, the figure reveals distinct and economically interpretable patterns across the exogenous variables. Higher air temperature and global horizontal irradiance are

associated with fewer bids and a weaker concentration around low prices, reflecting reduced residual demand when heating needs decline or solar output increases. Wind speed exhibits a non-monotonic effect: bidding activity peaks around moderate speeds (2–4 m/s) and declines at higher speeds, where increased volatility, curtailment risks, and stronger merit-order effects discourage producers from submitting bids except at very low prices. Fuel prices also display nonlinear associations with offered volumes, consistent with the heterogeneous marginal costs of the underlying producer mix. These relationships further justify the choice of contextual features for conditioning the DDPM and illustrate the type of structure that the model must learn from fully anonymous bid data.

For the supply side, the context variable \mathbf{X}^S in (4) consists of the Coal, Oil, and Gas prices reported in Table 3, while for the demand side, we take the temperature statistics.

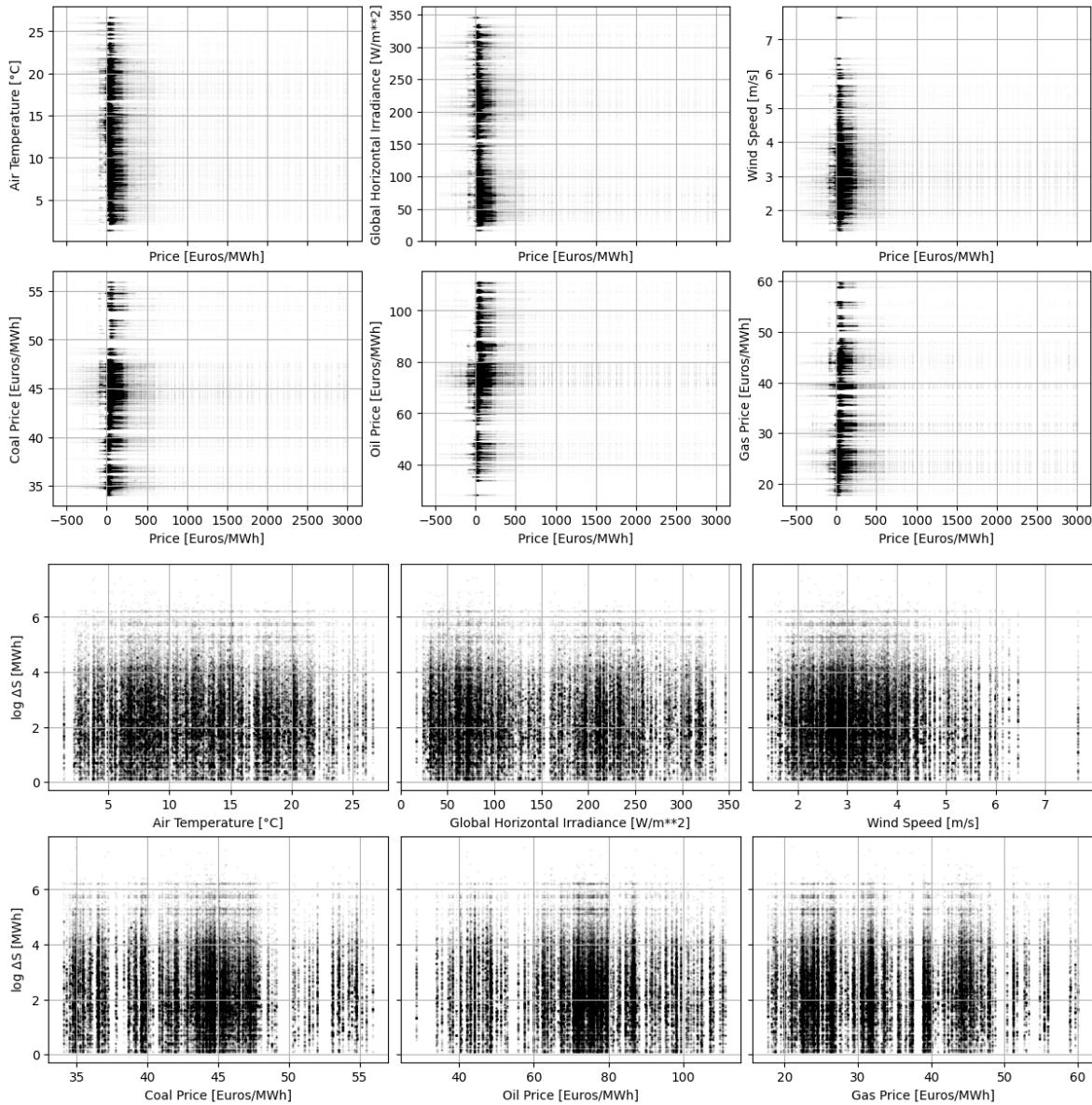


Figure 21: Arrival prices and offers ΔS against weather variables and fuels prices, year 2020

We use the EPEX SPOT supply curves for 2019 and 2020, obtaining 699 158 data points in dimen-

sion 37. The first 24 entries correspond to the sequence ΔS and the remaining 13 to P and the 12 selected features. We train the model for 5×10^2 epochs with a batch size of 256. Training time was 2 hours per model.

After training, and given a label \mathbb{X}^S together with a price P , the DDPM produces a 24-dimensional vector of volume marks

$$\Delta \tilde{S} = (\Delta \tilde{S}^1, \dots, \Delta \tilde{S}^{24}).$$

Because zero volumes were randomized during training using low-variance Gaussian perturbations, some generated components $\Delta \tilde{S}^i$ may take negative values. These negative values reflect artifacts of the Gaussian noise rather than genuine supply volumes. Accordingly, we truncate them to zero. Operationally, this amounts to interpreting a negative $\Delta \tilde{S}^i$ as the absence of an offer at hour i for the given label.

Figure 22 displays a generated sample of marks, $\Delta \tilde{S}$, obtained conditional on the real price sequence $(P_m)_{m=1}^{975}$ from 2020-10-05 (shown in Figure 15). In this plot, we isolate the behaviour of the second-stage model: rather than using synthetic prices produced by the first DDPM model, we fix the labels to the real prices and generate only the increments $(\Delta \tilde{S}_m)_{m=1}^{975}$. Despite the offers not showing the same pattern as the real ones, we observe some pattern preservation across hours, including block orders, similar to the case with real data. For the demand side, we obtain 783 189 data points in dimension 28, with the first 24 entries corresponding to ΔD and the remaining 4 to P and the temperature features.

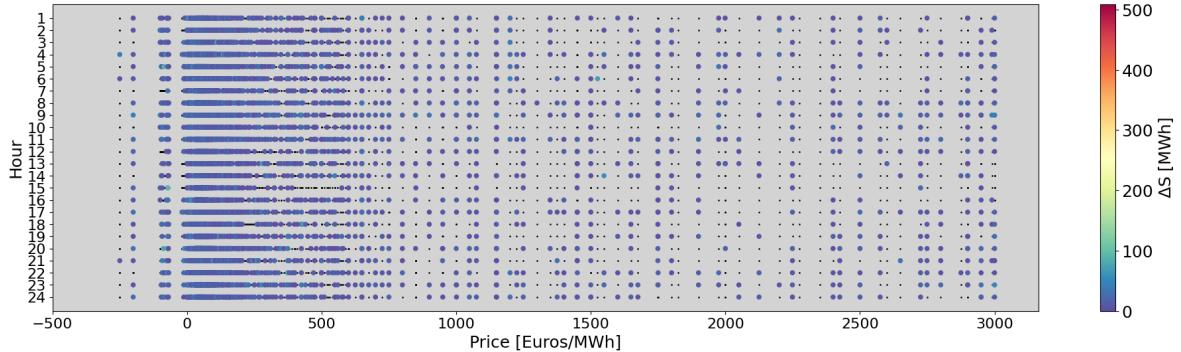


Figure 22: $(P_m, \Delta \tilde{S}_m)_{m=1}^{975}$ generated for 2020-10-05. Black dots represent 0-values on $\Delta \tilde{S}$.

3.2. Results

To assess the performance of the models introduced in Sections 3.1.1 and 3.1.2, we focus on generation results for a particular date. Figure 23 compares the observed curves, those predicted by the fast baseline models, and 200 curve samples from the generative models. As shown in the figure, the generated curves reproduce the switching between inelastic and elastic regimes with greater accuracy than the fast model. In particular, the elastic region exhibits the sharp slope of the observed curves. In the plateaus at high price levels (from 500 EUR onwards), some curves reach a plateau whose magnitude varies, sometimes underestimating and sometimes overestimating the observed value. In contrast, the fast models excel at recovering these plateau values. To quantify this, we compute the MSE error between each sample and the observed curve. Specifically, denoting by $p \mapsto S(p)$ and $p \mapsto \tilde{S}^j(p)$ the real and j sample of the generated supply curves, we interpolate them on a common grid with 1-euro spacing over the range $[-500, 3000]$. For each price tick p_k we compute

$$\text{Normalized MSE}(p_k) = \frac{1}{200} \sum_{j=1}^{200} \frac{(S(p_k) - \tilde{S}^j(p_k))^2}{S(p_k)^2}.$$

We carry out similar computations for the demand curves. Figure 24 displays the normalized MSE statistics computed over 200 samples. The results show negligible error in the negative price range

$[-500, 0]$, which is expected since the sample curves are anchored to the observed value at -500 EUR. Importantly, no abnormal offers appear in this range, so the initial inelastic regime at negative prices is preserved. In the elastic region, the error increases, stabilizing as the curves enter the plateaus at high price values. The average normalized MSE stays below 1.3% (5% for the demand), reaching at most 4% (20% for the demand) in extreme cases. Compared with the fast model, the following patterns emerge. The fast model captures both the low- and high-price plateaus, but its error tends to rise earlier in the elastic region before decreasing again as accuracy improves in the high-price range. The generative samples, by contrast, display more stable errors in the elastic region due to their sharper slope; yet, they incur higher errors in the high-price plateau as accuracy varies across samples. Remarkably, although the generative model operates only at the order level and never sees the entire curve, its aggregated orders still reproduce the inelastic–elastic regimes with high fidelity.

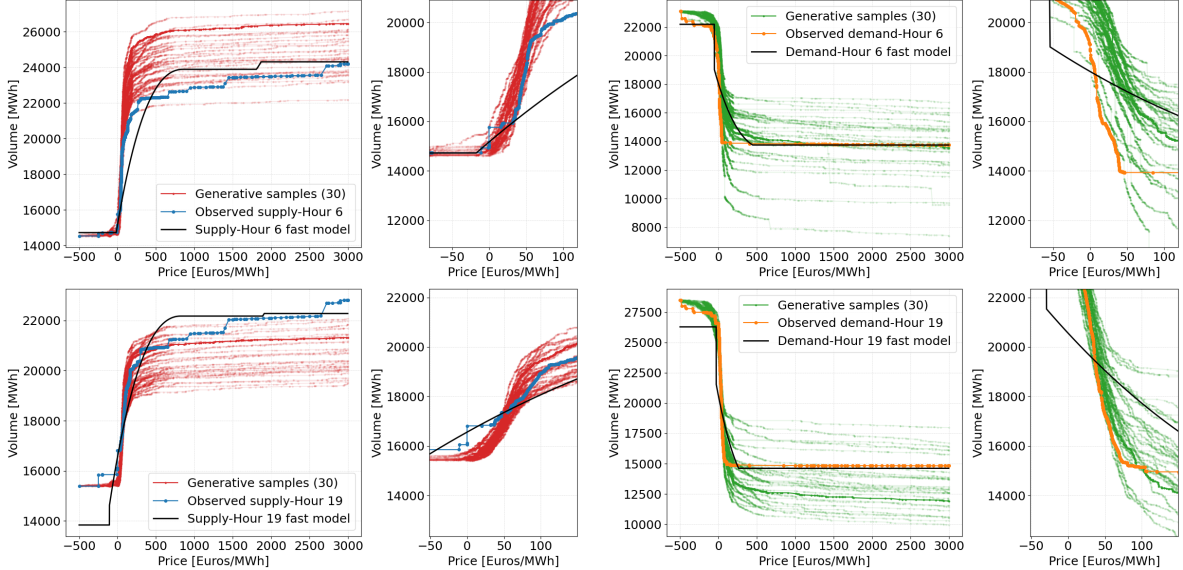


Figure 23: Observed, fast model, and generative model curves for hours 6 and 19 on 2020-10-05 (zoomed view on the right). Supply curves are shown on the left, and demand curves on the right.

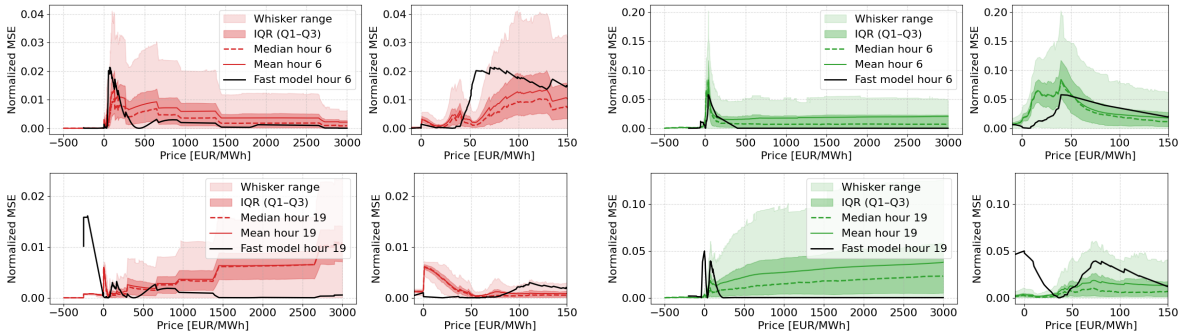


Figure 24: Normalized MSE statistics computed over 200 samples on 2020-10-05. (Zoom at price range $[-10, 150]$). Supply results are shown on the left, and demand results on the right.

To further evaluate the model’s performance, we examine the empirical joint and marginal distributions. For January 2020, we obtain a qualitative comparison by computing Gaussian kernel density estimates (KDEs) for the real data, the Fast model predictions, and a sample from the generative

model. Using Gaussian KDEs for visual sample comparison provides a smooth, continuous approximation of empirical distributions, making features such as modality, skewness, tail behaviour, and relative differences between datasets more discernible than with discrete histograms. The analysis focuses on hours 6 and 20, and on the price range $[-300, 1200]$, though it can be extended to all hours and the full price range.

We begin with the marginal distributions of feature-volume pairs. The Fast model, though not conditioned on the same features, is used as a reference. Figure 25 shows Gaussian KDEs for the feature–volume marginals corresponding to Gas price and GHI for one generated sample. Similar patterns are observed for the remaining features. We also examine the marginal distribution of price–volume pairs. Figure 26 presents the Gaussian KDEs of these pairs.

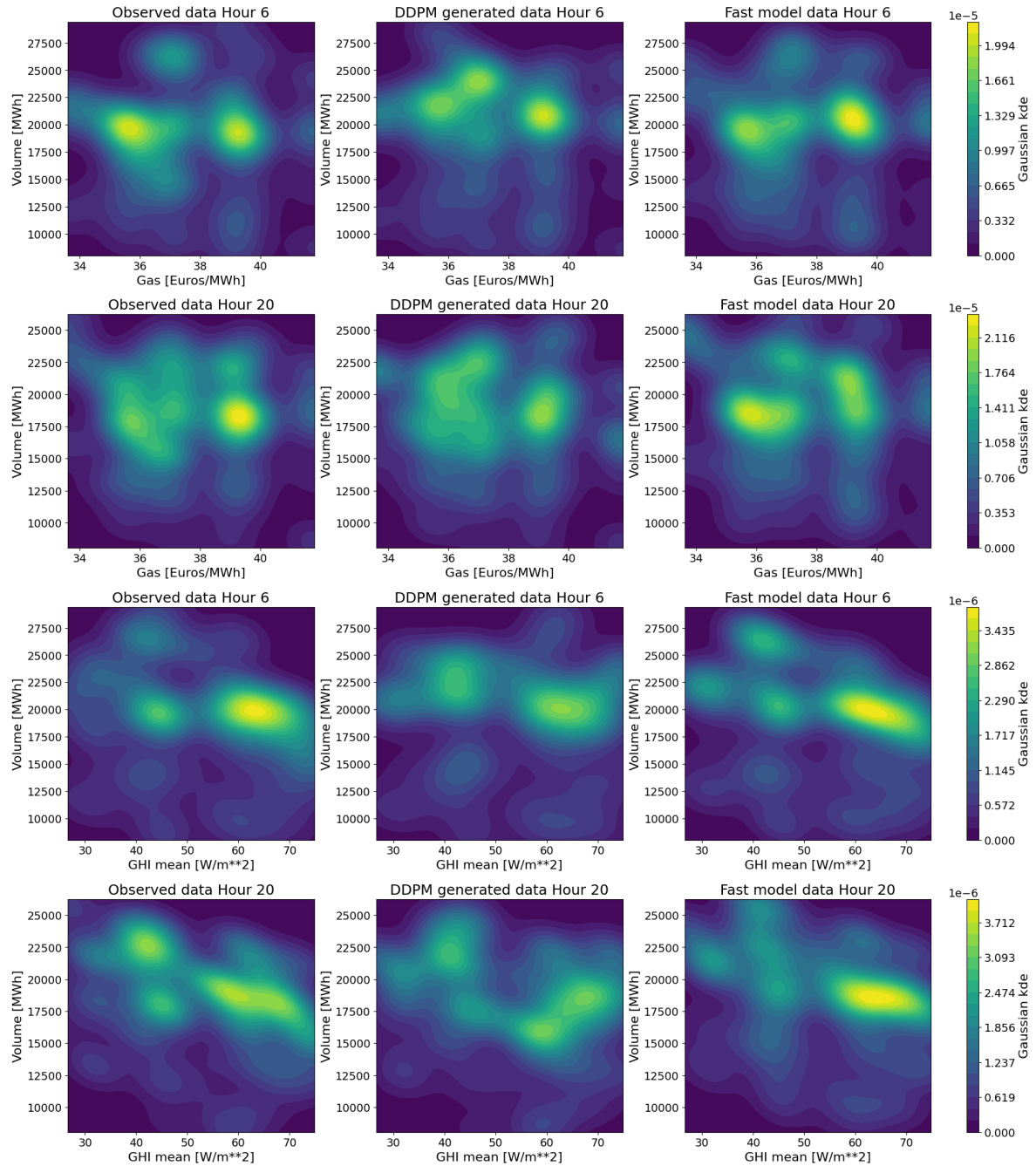


Figure 25: Gaussian KDEs of the feature–volume distribution from data, a DDPM-generated sample, and the fast-model prediction for hours 6 and 20 on January 2020. Only the Gas price and GHI mean are illustrated.

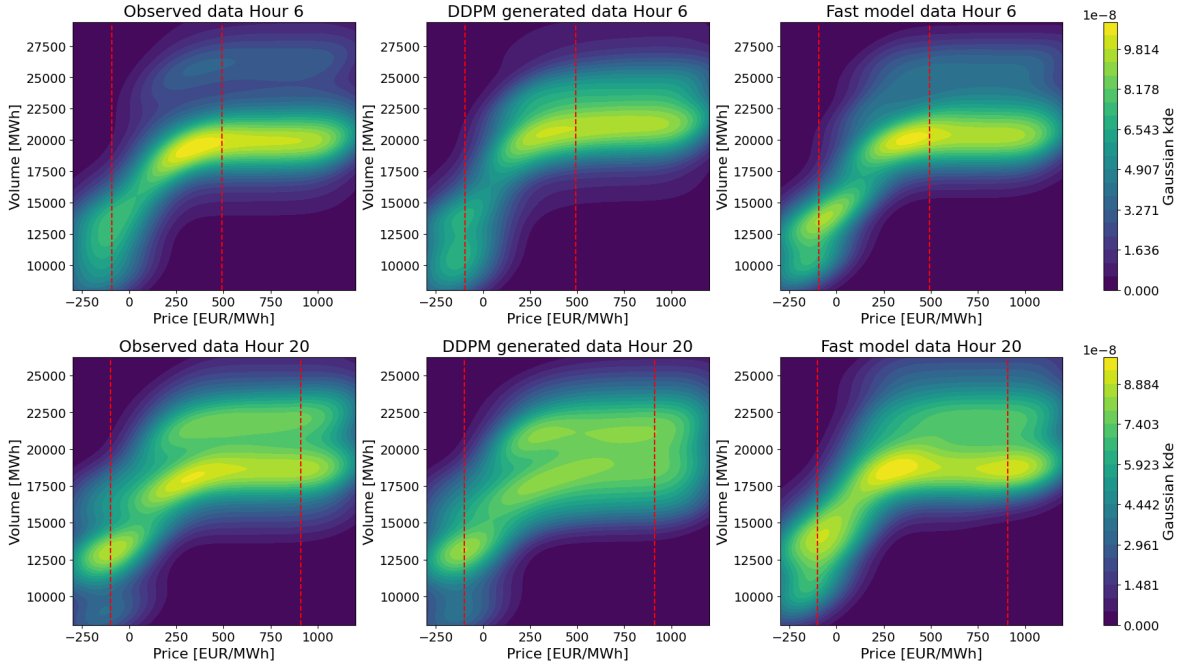


Figure 26: Gaussian kernel density estimates (KDEs) of the price-volume distribution for data, a DDPM-generated sample, and the Fast model prediction at hours 6 and 20 on January 2020. Red vertical lines delimit the elastic and plateau regions for each hour obtained by the Fast model.

We complement the qualitative comparison offered by the KDEs using a quantitative metric: the Wasserstein distance between the corresponding sample distributions Galichon (2016); Peyré and Cuturi (2019); Peyré (2025). The Wasserstein distance provides a way to compare probability distributions through optimal transport. In the empirical setting, we observe finite point clouds $\mu_n = \frac{1}{n} \sum_{i=1}^n \delta_{x_i}$ and $\nu_m = \frac{1}{m} \sum_{j=1}^m \delta_{y_j}$, possibly with different sample sizes $n \neq m$. The Wasserstein distance is obtained by solving the discrete optimal transport problem

$$W_2^2(\mu_n, \nu_m) = \min_{\pi \in \Pi(\mu_n, \nu_m)} \sum_{i=1}^n \sum_{j=1}^m \pi_{ij} \|x_i - y_j\|^2,$$

where $\Pi(\mu_n, \nu_m)$ is the set of transport plans with row and column sums matching the empirical weights. Here, the distributions are compared by relocating the observed mass at the sample points, so the distance reflects both how far points must be moved and how much mass is transported. A primary limitation of the Wasserstein distance as a similarity metric is the lack of a clear threshold for determining when two distributions are sufficiently close. We therefore use the Fast model as a benchmark.

The first Wasserstein distance is between the joint sample distribution of hours 6 and 20, volumes, prices, and features—Coal, Oil, and Gas prices, mean AT, GHI, and WS. To assess the stability of the DDPM samples, we repeat the computation over 100 generated samples for the same period of January 2020. Figure 27 shows that the metric is stable, with an interquartile range of about 2 % of its mean. However, the DDPM does not exceed the performance of the Fast model.

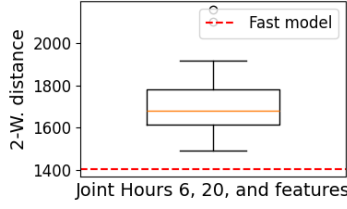


Figure 27: Boxplot of the Wasserstein distance to data across 100 generated samples and Fast model prediction.

Since projection functions are 1-Lipschitz, the Wasserstein distance between joint distributions provides an upper bound for the distances between their marginals. To examine the contribution of each marginal to the joint distance, we compute Wasserstein distances separately across price regimes. Specifically, we partition the datasets into elastic and plateau regions according to the boundaries determined by the Fast model. For hour 6, the elastic region corresponds to prices between -93.93092 and 492.79517 , defined by the maximum of the plateau starting values and the minimum of the plateau ending values for the January period. For hour 20, the corresponding limits are -100.14883 and 909.5548 . This subdivision is justified because both the Fast and DDPM models reproduce the elastic and plateau behaviours, though the curve dynamics differ across these regimes. Figure 26 indicates the price boundaries used for this partition with vertical dotted red lines.

For price-volume pairs, Figure 28 shows that only at hour 20 and in the elastic region are the DDPM-generated samples closer to the real data than the Fast model. Otherwise, the Fast model outperforms the DDPM model. As for the features, Figure 29 reports the Wasserstein distances for Gas and GHI. Similar results are observed across the remaining features. We observe that Gas and GHI play a role in both elastic and plateau price regions only for hour 20.

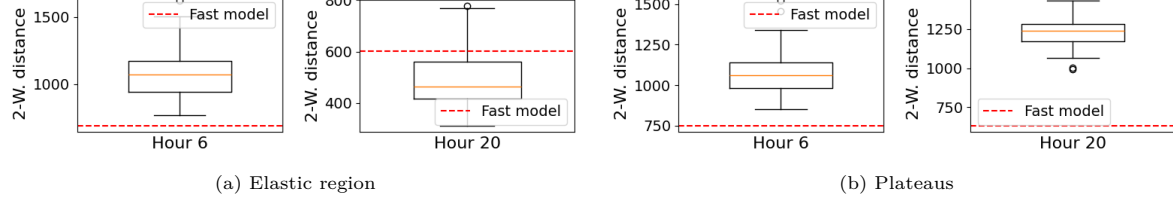


Figure 28: Boxplots of Wasserstein distance comparing DDPM generated samples and fast-model predictions to data on price-volume pairs for hours 6 and 20 on January 2020.

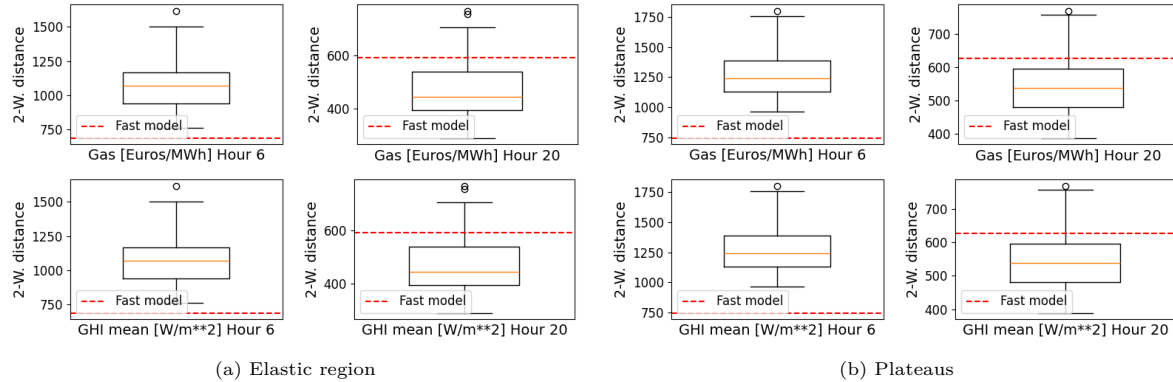


Figure 29: Boxplots of Wasserstein distance comparing generated samples and fast-model predictions to data on feature-volume pairs for hours 6 and 20 on January 2020. Only Gas and GHI are reported.

Overall, the results indicate that the generative model accurately captures both the joint and marginal distributions, and that the conditioning features exert a meaningful influence on the generated samples. Nevertheless, on average, the generative model does not consistently outperform the deterministic Fast model. This analysis, however, helps identify the features to focus on to improve the generative model's performance.

4. Optimal strategy of a price-maker storage agent

Based on forecasts of the demand and supply curves, we study in this section the optimal strategy of a price-maker storage agent. A further objective is to investigate how storage influences the day-ahead electricity price, as storage is one of the main sources of flexibility to mitigate the widening price spreads driven by renewable energy uncertainty.

4.1. Price impact model of storage

In this section, inspired by Supply Function Equilibrium models, we define for any hour h and day d , the non-increasing demand function $P \mapsto D_{d,h}(P)$ and non-decreasing supply function $P \mapsto S_{d,h}(P)$. In SFE models, firms choose entire supply functions mapping prices to quantities, and an equilibrium is a profile of such functions that is profit-optimal for each firm given the residual demand and the rivals' supply functions. We say that the market-clearing condition holds when the following is true:

$$D_{d,h}(P) = S_{d,h}(P), \quad h = 1, \dots, 24, \quad d > 0.$$

The drawback of deriving the optimal strategy of an agent from forecasts is the gap between prediction and reality. To account for this, we introduce an auxiliary variable X , representing the prediction error on the net supply and demand. Since X depends on the difference between the renewable prediction and the actual production, for any $h = 1, \dots, 24$ and day d , $X_{d,h}$ is a random variable and we make the following assumption:

Assumption 4.1. *For any $h = 1, \dots, 24$ and day d , $X_{d,h}$ admits a density $\pi_{d,h}$ and takes values in \mathbb{R} . Moreover, the $(X_{i,j})_{i,j}$ are independent.*

In the present framework, we select two hours that are sufficiently far apart (e.g., an off-peak and a peak hour), so that the corresponding forecast errors are expected to exhibit weak dependence. Empirically, such hour pairs behave close to independent, which supports Assumption 4.1 and simplifies the computation of expected revenues. If independence is dropped and a general joint law for (X_1, X_2) is allowed, the maximization problem remains well posed, but the economic outcome may change: different dependence structures modify the frequency of profitable spreads and can substantially affect expected revenues. In stochastic optimization, this discrepancy between analyses with and without independence is known as the correlation gap Agrawal et al. (2010, 2012).

We now fix an arbitrary day d , and to simplify the notation, we omit the index d whenever it is not required. For ease of exposition, we continue to work with two representative hours, denoted 1 and 2 (e.g. an off-peak and a peak hour), and focus on a single spread between these hours. The storage agent chooses how much energy to shift between hour 1 and hour 2, but the hours themselves are taken as given: we do not optimise over the set of hours. A natural extension would be to allow blocks across multiple optimally selected hours. We consider a storage agent aiming to determine its optimal trading strategy across these two hours. In practice, this strategy is implemented as a block order: the agent withdraws a quantity $q(P_1, P_2)$ at hour 1 and injects the same amount at hour 2, profiting from the price difference. The orders will be triggered only when specific conditions on the price on both hours are met. The transfer quantity q is non-negative and bounded above by a technical limit q_M . Since the agent does not observe the true supply and demand curves, the decision is based on predicted ones. The resulting market-clearing conditions are

$$S_1(P_1) + X_1 = D_1(P_1) + q(P_1, P_2), \quad S_2(P_2) + X_2 + q(P_1, P_2) = D_2(P_2), \quad (6)$$

respectively. Because $X = (X_1, X_2)$ captures the forecasts errors, the equilibrium prices P_1 and P_2 are random variables determined by the realizations of X . Accordingly, the supply and demand functions S_i and D_i , $i = 1, 2$ in (6), can be regarded as deterministic functions of price, which in turn depends on the random variable X . This formulation makes it possible to optimize over price functions $X \rightarrow P_1(X), P_2(X)$. For $i = 1, 2$, S_i and D_i are deterministic functions that depend, through price, on a random variable. The storage agent aims at maximizing its expected revenues:

$$\mathbb{E}[q(X_1, X_2)(P_2(q(X_1, X_2), X_2) - P_1(q(X_1, X_2), X_1))] \quad (7)$$

It is convenient to define the following functions:

$$\begin{cases} \Gamma_1(P) := D_1(P) - S_1(P) \\ \Gamma_2(P) := D_2(P) - S_2(P) \end{cases} \quad (8)$$

which measure the difference between demand and supply at price P , for which we assume the following:

Assumption 4.2. Γ_1 and Γ_2 are C^1 and decreasing functions.

For clarity, we assume that Γ_i are decreasing, but the arguments remain valid (with minor modifications) if they are only non-increasing. The assumption guarantees the invertibility of Γ_i and thus uniqueness of the equilibrium price for each realization of the forecast error. For each (x_1, x_2) , let $P_i^{x_i}(q) := \Gamma_i^{-1}(x_i + (-1)^i q)$. Then, for any given pair (x_1, x_2) , define $f(\cdot; x_1, x_2) : q \mapsto q(P_2^{x_2}(q) - P_1^{x_1}(q))$. We have the following theorem:

Theorem 4.1 (Existence). *Suppose that Assumptions 4.2 and 4.1 hold. There exists an optimal function q^* that maximises (7).*

Proof. Since Γ_i , $i = 1, 2$, are C^1 and decreasing, and prices lie in a compact interval, $(\Gamma_i^{-1})_i$ are continuous and take values in that interval. Hence, for each (x_1, x_2) , $f(\cdot; x_1, x_2)$ is continuous on $[0, q_M]$, so a maximizer exists. Moreover, there exists $C > 0$ such that

$$|f(q; x_1, x_2)| = |q(P_2^{x_2}(q) - P_1^{x_1}(q))| \leq C,$$

so there exists $C' > 0$ such that $\int \sup_{q \in [0, q_M]} |f(q, x_1, x_2)| \pi_1(x_1) \pi_2(x_2) dx_1 dx_2 \leq C'$. Using a classical supremum-integral exchange argument, the supremum over measurable policies equals the integral of pointwise suprema. \square

With Assumption 4.2, $(P_i^{x_i})_i$, $i = 1, 2$ are continuous on $(0, q_M)$ and we define

$$g(q; x_1, x_2) := \frac{\partial f}{\partial q}(q; x_1, x_2) = (P_2^{x_2}(q) - P_1^{x_1}(q)) + q \left(\frac{1}{\Gamma_2'(P_2^{x_2}(q))} + \frac{1}{\Gamma_1'(P_1^{x_1}(q))} \right),$$

which we extend by continuity to q_M .

Having established the existence of an optimal policy, we now turn to its characterization. For each realization of the forecast errors (x_1, x_2) , the storage agent's problem reduces to the maximization of $f(q; x_1, x_2)$ over $[0, q_M]$. The solution, therefore, lies at one of the boundaries or corresponds to an interior point characterized by the first-order conditions. This is summarized in the following proposition.

Proposition 4.1 (Characterization of the optimal strategy). *Suppose that Assumptions 4.1 and 4.2 hold. Any maximizer $q^* \in [0, q_M]$ satisfies exactly one of the following:*

- (lower corner) $\Gamma_2^{-1}(x_2) - \Gamma_1^{-1}(x_1) \leq 0$ and $q^* = 0$,
- (upper corner) $g(q_M) \geq 0$ and $q^* = q_M$

- (interior solution) $q^* \in (0, q_M)$ and

$$P_2^{x_2}(q^*) - P_1^{x_1}(q^*) = -q^* \left(\frac{1}{\Gamma'_2(P_2^{x_2}(q^*))} + \frac{1}{\Gamma'_1(P_1^{x_1}(q^*))} \right) \quad (9)$$

The proof is clear by differentiating f and using the Karush-Kuhn-Tucker conditions. These conditions become sufficient if f is a concave function of q .

We distinguish two complementary representations of the storage strategy. For ex-ante evaluation, we work in the (x_1, x_2) space (forecast errors), whose joint distribution is known; the optimal policy is obtained pointwise as $q^*(x_1, x_2)$ via Proposition 4.1, which allows us to compute expected revenues, examine profit distributions. For market implementation, bids must be presented as price-quantity schedules, so we express the strategy in terms of prices. Equation (9) yields following corollary:

Corollary 4.1 (Price-form of the optimal strategy). *Suppose that Assumptions 4.2 and 4.1 hold. Then the solution can be expressed in a price-dependent form:*

$$q_{\text{int}}(P_1, P_2) = \frac{P_1 - P_2}{\frac{1}{\Gamma'_2(P_2)} + \frac{1}{\Gamma'_1(P_1)}}, \quad q(P_1, P_2) = \min\{\max\{q_{\text{int}}(P_1, P_2), 0\}, q_M\}.$$

4.2. Applications and Case Study

In this section, we study a storage unit operating in the day-ahead market in two parts. First, we consider a day-to-day analysis relevant for a trader, using the forecasts developed in Section 2 with our fast baseline model. Second, we provide a comprehensive study, based on the forecasts from Section 3, of the impact of storage on the market (on prices, profitability, and strategy robustness). This broader perspective reflects the needs of a TSO or of a trader interested in deeper analyses that do not need to be performed every day before market closure. To illustrate the analysis of trading strategies in the framework of Section 4.1, we present a case study of arbitrage opportunities between an off-peak hour (05:00) and a peak hour (19:00) for 2020-10-05.

Calibration of X . To implement the framework of Section 4.1, the first step is to calibrate X . Define $D_{d,h}^{\text{pred}}$ and $S_{d,h}^{\text{pred}}$ to be a prediction of demand and supply curves $D_{d,h}$ and $S_{d,h}$, respectively. We assume that the prediction error X corresponds to the imbalance between predicted demand and predicted supply at the observed market price. More precisely, for an hour h and a date d , we denote by $P_{d,h}^{\text{obs}}$ the observed market price, then $X_{d,h}$ is defined in this way:

$$X_{d,h} = D_{d,h}^{\text{pred}}(P_{d,h}^{\text{obs}}) - S_{d,h}^{\text{pred}}(P_{d,h}^{\text{obs}}). \quad (10)$$

This definition assesses the prediction models exactly where accuracy matters the most: at the market-clearing price. The intuition is that the misprediction of renewables mainly drives the forecast errors. Each forecasting framework, whether the fast one described in Section 2 or the generative one described in Section 3, has its own calibration of X , as it is linked to the distribution of errors. In practice, for a fixed h , each realization of $X_{d,h}$ is treated as a sample of a random variable observed across multiple days within a given time horizon. This allows the error distribution to be considered hour-dependent only, since realizations for the same hour h across different days are assumed to follow the same distribution π_h . This gives one random variable per hour. We calibrate X from observed market prices and the corresponding predicted demand and supply curves over the period 2020-01-01 to 2020-08-31. From the resulting dataset $\{X_{h,d}\}$, we estimate their marginal distribution $\pi_h(x)$, $h = 1, \dots, 24$. We select the distribution of X by minimizing the BIC (Bayesian Information Criterion), considering the Gaussian, Student-t, Laplace, generalized normal (gennorm), skew-normal, and Cauchy families.

4.2.1. Day-to-day analysis using the fast model

For the selected hours, 5 and 19, the empirical distributions of X is, according to the BIC criteria, approximated with $X_{d,5} \sim \mathcal{N}(\mu_5, \sigma_5)$ and $X_{d,19} \sim \text{Laplace}(\mu_{19}, b_{19})$, with the following estimated parameters:

$$\begin{aligned}\mu_5 &= 555\text{MW}, & \sigma_5 &= 2300\text{MW}, \\ \mu_{19} &= 1367\text{MW}, & b_{19} &= 1896\text{MW}.\end{aligned}$$

Figure 30 shows the quantile-quantile plots comparing the theoretical distributions with the empirical data for $X_{d,5}$ and $X_{d,19}$, providing a visual assessment of the goodness-of-fit.

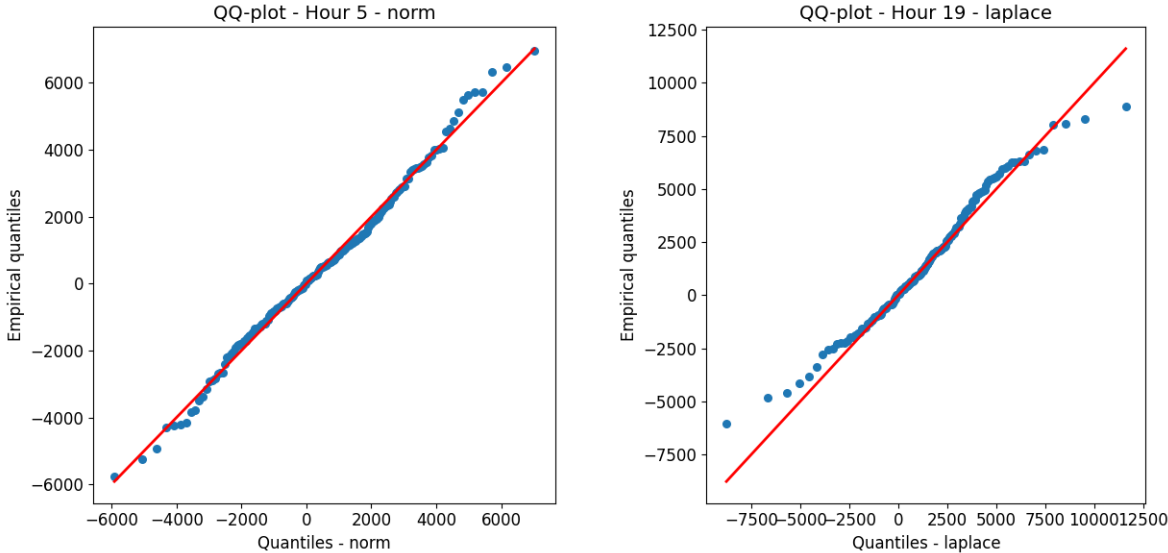


Figure 30: quantile-quantile plots of $X_{d,5}$ and $X_{d,19}$ versus their fitted distributions

Numerical illustrations of optimal strategies. Now that X has been calibrated, we implement the model of Section 4.1 for a case study on 2020-10-05, where the storage agent performs arbitrage between the off-peak hour (05:00) and the peak hour (19:00). We fix the maximum withdrawal rate $q_M = 1\,000\text{MW}$ and solve equation (9) using the `brentq` function from `scipy.optimize`. Figure 31 shows the surface $q(x_1, x_2)$ for truncated values of (x_1, x_2) . As anticipated, the constraints are most often binding. The surface splits into three regions:

- In the upper-left region, arbitrage is not profitable, and the optimal decision is $q^* = 0$.
- In the lower-right region, the opposite holds: it is profitable to inject at full capacity because the spread remains positive, so $q^* = q_M$.
- Between these two regions lies a smooth boundary, where the storage's price impact becomes relevant. Along this boundary, excessive injection would turn the spread negative, hence the need to choose a value between 0 and q_M .

The intermediate region, derived from the first-order conditions, disappears in a model that ignores price impact. As illustrated in Figure 32, an agent without price impact considerations follows a naïve strategy: charging at full capacity during off-peak hours and discharging at full capacity during peak hours whenever the spread is positive. This behavior overlooks the agent's own price impact and thus omits the transition region captured by the price impact model.

This difference between strategies affects revenues in two ways. Figure 33 and 34 show the distribution of revenue of the agent, computed on 10 000 samples of X , on both strategies. Firstly, in the naïve case, the agent may occasionally incur negative revenues due to the transition region described above, which an agent accounting for price impact would avoid. Secondly, it lowers the average revenue (from approximately 30 000 to 22 000 EUR), leading to a $\approx 27\%$ decrease in average value in the naive model compared to our model of price impact.

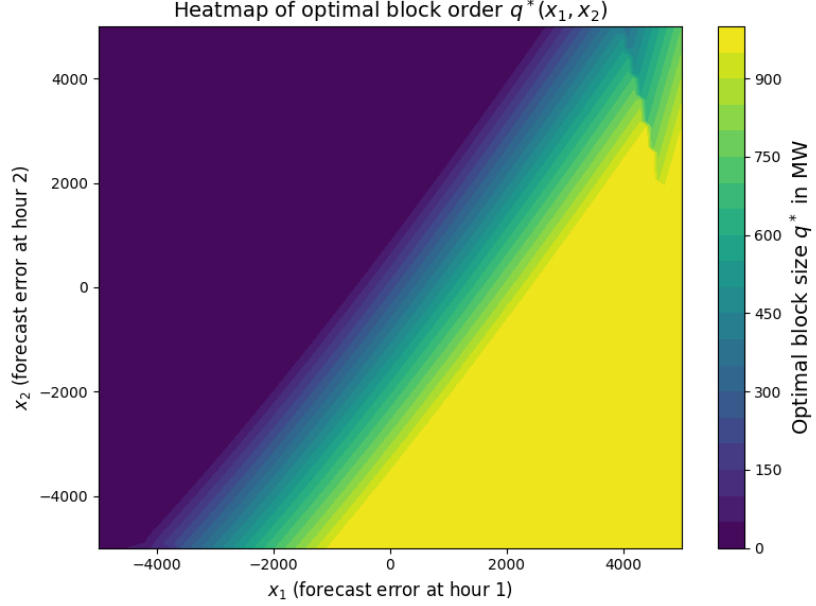


Figure 31: Optimal block size q^* as a function of (x_1, x_2) .

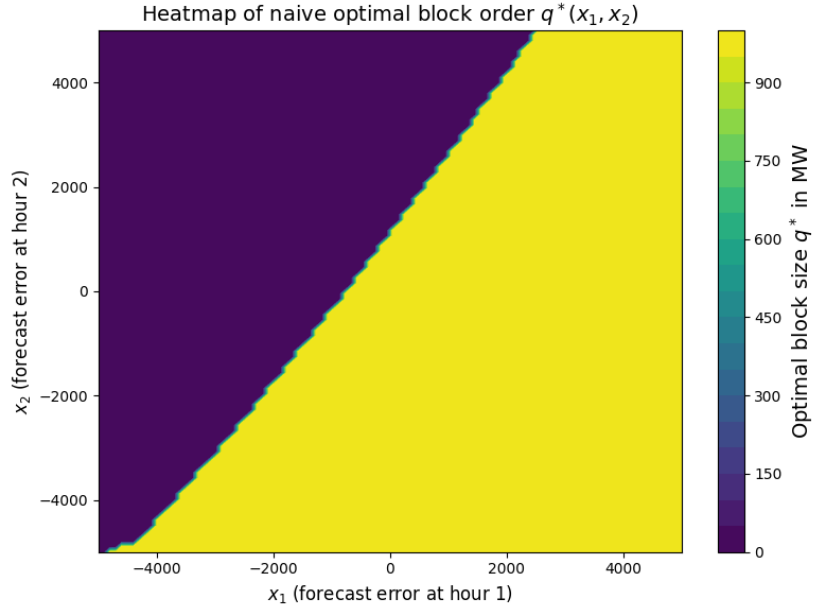


Figure 32: Naive optimal block size q^* as a function of (x_1, x_2) .

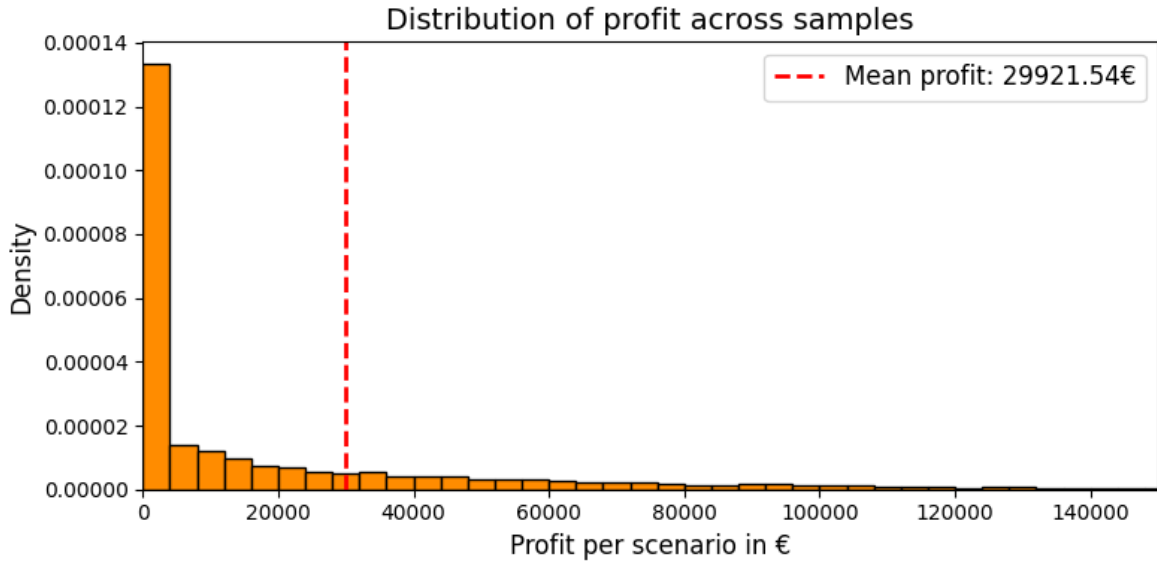


Figure 33: Distribution of the revenues of a storage with a maximum withdrawal rate of 1000 MW in our model, computed over 10 000 samples of X .

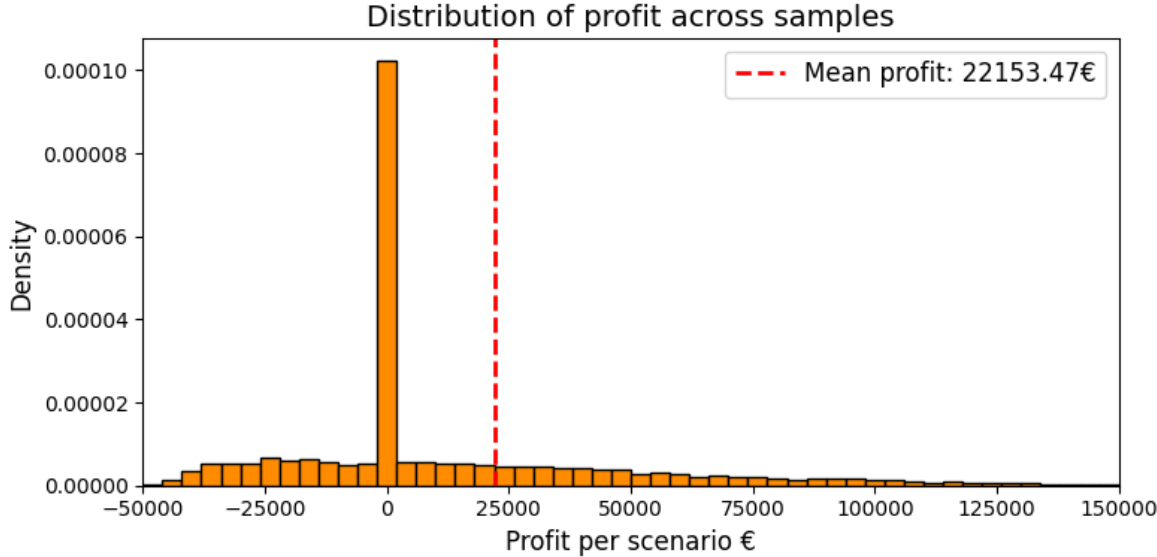


Figure 34: Distribution of the revenues of a storage with a maximum withdrawal rate of 1 000 MW in the naive case, computed over 10 000 samples of X .

Impact of the storage agent's strategy on the spread. It is interesting to put these results into perspective, not only from the storage agent's point of view but also in terms of the visible impact on prices that his action would have. Figure 35 shows the change in spread caused by the storage's strategy for any couple (x_1, x_2) . While $q^*(x_1, x_2)$ in Figure 31 displays the optimal block size, the impact heatmap quantifies the market footprint of executing that order. If we compare with Figure 31, both exhibit the same pattern along the diagonal and top-left corner. Away from this area, storage compresses the

spread and, for a small q , the magnitude is governed by local price elasticities:

$$\Delta\text{Spread}(q) = (P_2(q) - P_1(q)) - (P_2(0) - P_1(0)) \approx q \left[\frac{1}{\Gamma'_2(P_2(0))} + \frac{1}{\Gamma'_1(P_1(0))} \right] \leq 0$$

In this regime, the impact on the spread is proportional to q and depends solely on the slopes $\Gamma'_2(P_2(0))$ and $\Gamma'_1(P_1(0))$. For greater q , this expression becomes non-linear, explaining the stronger variability compared with Figure 31.

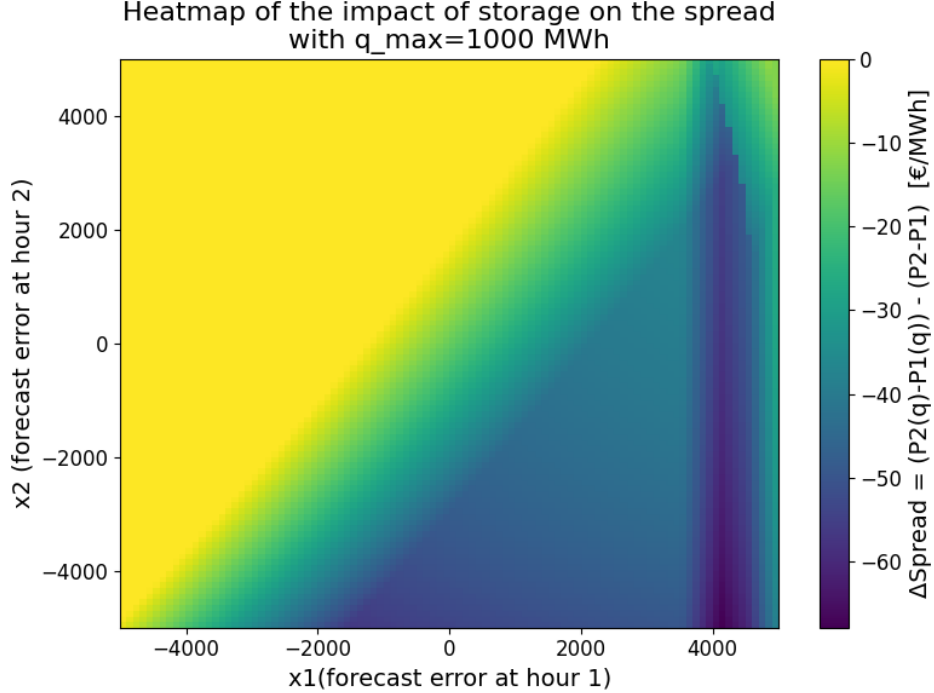


Figure 35: Heatmap of the impact of the storage on ΔSpread .

4.2.2. Profitability analysis using the generative model

We calibrate X against the generative model, taking $S_{d,h}^{\text{pred}}$ and $D_{d,h}^{\text{pred}}$ as the mean of 10 supply and demand curves generated in Section 3. This choice reduces algorithmic complexity during calibration. However, in the equilibrium equation (6), we will work with averages over 100 generated samples. This choice of using the average curve will be further discussed at the end of this section. Following the same procedure to fit the best distributions (by the BIC criteria) as in the beginning of Section 4.2.1, we find that $X_{d,5} \sim \text{SkewNorm}(a_5^g, \mu_5^g, \sigma_5^g)$ and $X_{d,19} \sim \text{SkewNorm}(a_{19}^g, \mu_{19}^g, \sigma_{19}^g)$ with

$$\begin{aligned} \mu_5^g &= 1149\text{MW}, & \sigma_5^g &= 6680\text{MW}, & a_5^g &= 4.86 \\ \mu_{19}^g &= 2265\text{MW}, & \sigma_{19}^g &= 5466\text{MW}, & a_{19}^g &= 3.65. \end{aligned}$$

Figure 36 shows the quantile-quantile plots comparing the theoretical distributions with the empirical data for $X_{d,5}$ and $X_{d,19}$, providing a visual assessment of the goodness-of-fit.

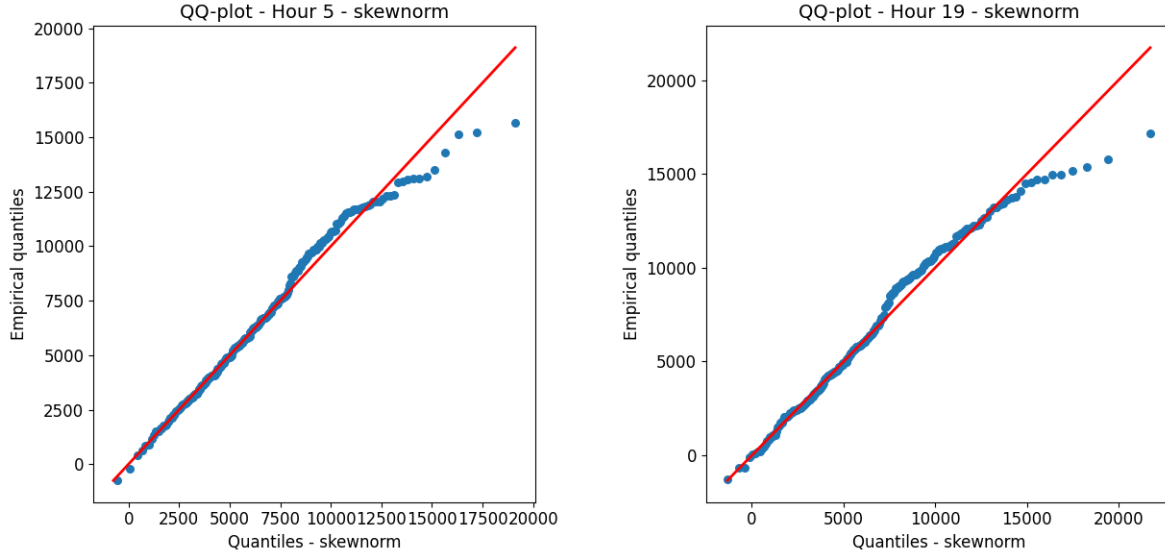


Figure 36: quantile-quantile plots of $X_{d,5}$ and $X_{d,19}$ versus their fitted distributions

Comparison of the revenue distribution. We compare the fast and generative models by examining what revenues would have been if the generative model had been used operationally on a day-to-day basis. Figure 37 shows the revenue distribution under this choice. The first observation is that the average revenue obtained is 2 times higher (approx. 30 000 to 61 000 EUR), meaning that the fast model yields a smaller average revenue. The second observation concerns the shape of the distribution. An advantage of the generative model is that the distribution tails are lighter near zero, which translates into less uncertainty and fewer cases where revenues are close to zero. The fast model from Section 2 is suitable for day-to-day use but has the drawback of higher potential volatility in revenues, with a greater likelihood of smaller daily revenues.

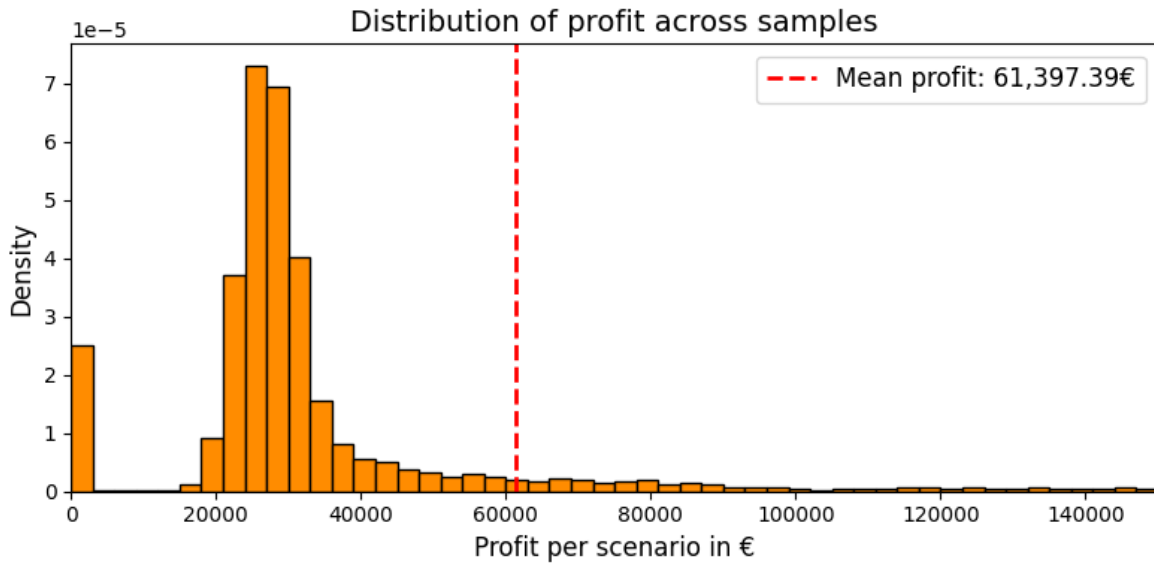


Figure 37: Distribution of the revenues of a storage with a maximum withdrawal rate of 1 000 MW, computed over 10 000 samples of X , using the generative model for the supply and demand curves.

Impact of storage on the electricity price. It may be of interest for a TSO or a storage owner to move beyond the price–spread impact at a fixed maximum storage level (Figure 35) and examine how the spread depends on the storage capacity. Indeed, the fact that storage reduces peak prices and increases off-peak prices is well established in the literature (see e.g., Dumitrescu et al. (2024); Shafiee et al. (2016)). Figure 38 shows the average (over 10,000 samples of X) change in hours 1 and 2, as well as in the spread, as a function of the storage capacity in the market. It highlights that more storage in the market leads to a price reduction, up to a point where the additional benefit becomes minimal. Beyond approximately 1500 MW of storage, we observe a form of cannibalization as in Dumitrescu et al. (2024) in the intraday market: the more storage is added, the smaller the impact of each additional capacity increase. This phenomenon will also be evident in the following paragraphs.

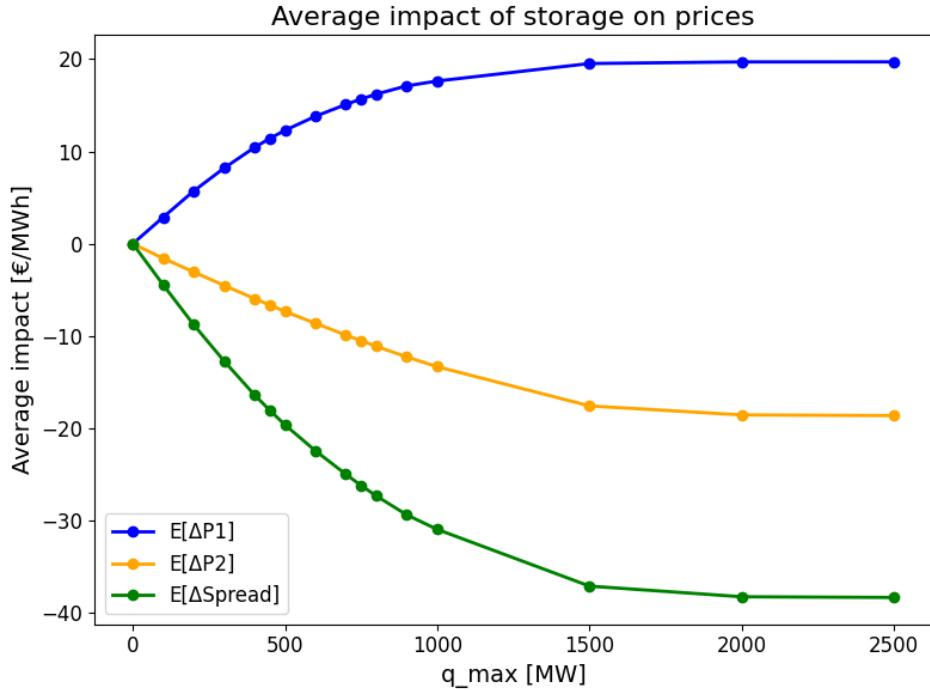


Figure 38: Average change in price for hours 1 (05:00), 2 (19:00), and for the spread, depending on storage capacity in the market, computed over 10 000 samples of X .

Profitability of increased capacity. For a storage asset owner, it is important to assess whether increasing the value of q_M would be profitable. According to BIELEWSKI et al. (2022), the price of a battery in Europe is about 150 EUR/kWh, and we assume that increasing the maximum storage capacity would proportionally increase the maximum quantity q_M . Figure 39 shows the time required to recover the cost of increasing the injection rate by 100 MW, depending on the current maximum rate. To estimate battery degradation over time, we add a degradation constant c_{deg} , which represents the cost per MWh transported. According to Preger et al. (2020), a battery can withstand between 2 500 and 9 000 cycles for the most recent technologies. Considering the cost of a battery in Europe, this corresponds to a cost per MWh injected/withdrawn of between 15 EUR/MWh and 60 EUR/MWh. For this application, we set $c_{deg} = 30$ EUR/MWh. Since this toy example only considers revenues over two hours out of 24, we simply allocate 2/24 of the dailyised additional capacity cost to these two hours, as a rough pro-rata of a fixed daily cost. Figure 39 shows that beyond $q_M = 1500$ MW, it would take more than 10 years to recover the added capacity cost, a duration that could reduce the attractiveness of the investment. The required payback time then increases almost exponentially with capacity. This finding is consistent with Figure 38, where we observed that beyond a certain capacity,

increasing the maximum storage has no further impact on price, meaning that marginal gains are very small.

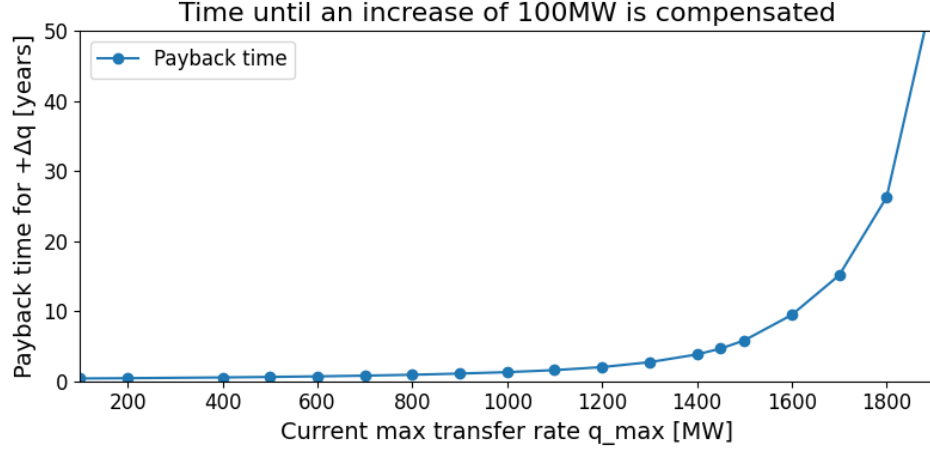


Figure 39: Evolution of the time required to recover the cost of increasing the injection rate by 100 MW depending on the current q_M

To explain the results on the payback time, we plot the share of scenarios where the q_M constraint is saturated and where an interior solution arises. However, beyond 1500 MW, the share of interior solutions dominates the share of saturated solutions: the higher the maximum capacity, the less often it will be binding, which mechanically reduces the opportunities to increase revenues by raising q_M .

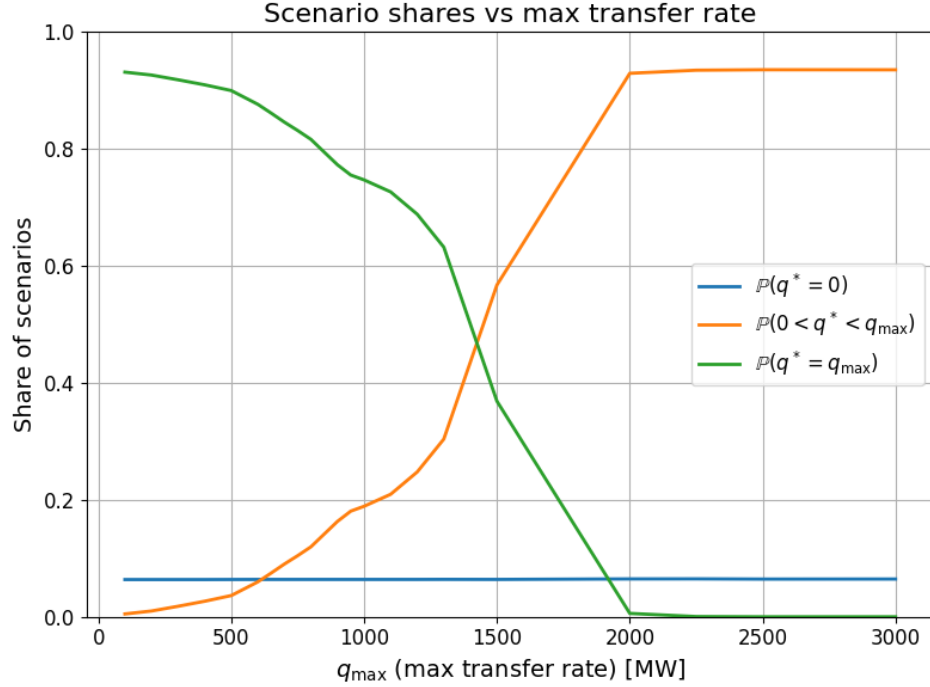


Figure 40: Shares of optimal decision regimes as a function of the maximum transfer rate q_M , computed over 10 000 samples of X . The green curve shows the share of scenarios where the transfer constraint binds ($q^* = q_M$), the orange curve corresponds to interior solutions ($0 < q^* < q_M$). The share of inactive storage is in blue.

Robustness to supply-side and demand-side scenarios. To evaluate the robustness of both the model and the storage strategy, we assess how sensitive the revenues are to the choice of supply and demand curves by comparing the strategy's performance under individual scenarios generated using the model of Section 3, by keeping the X calibration fixed but changing the supply and demand curves used in (6). The procedure consists of three steps:

- (i) We fix the optimal strategy based on the use of the average supply and demand curves in Equation (6), as described at the beginning of the current section.
- (ii) Compute the resulting average revenue over 10 000 samples of X .
- (iii) Repeat the calculation across many generated supply and demand scenarios, by changing the supply function S and the demand function D in Equation (6) and observe how the average revenue evolves.

The results are presented in Figure 41, which shows four panels of boxplots. In each panel, revenues are reported when three of the curves in (6) are fixed and the fourth one varies, across 100 generated scenarios. For instance, the bottom-right corresponds to D_1, D_2 , and S_1 kept fixed and S_2 varies. This comparison illustrates how strongly the strategy's profitability depends on the specific shape of the supply or demand curves. Beyond yielding higher revenues through the price impact model, the generative technique enables the assessment of the robustness of optimal storage strategies. It further shows that profits obtained under the policy optimized on the average demand and supply curves remain positive when accounting for both demand-side and supply-side variability. In fact, the profits under the average curves lie within the interquartile range and close to the median of the generated scenarios, justifying the choice made at the beginning of this section to take the average curve, as it delivers robust outcomes. Compared to the fast baseline model in the previous section, the generative framework enriches the profit variability study by providing a deeper analysis of robustness and sensitivity under scenario uncertainty, highlighting how demand- and supply-side drivers shape the revenue distribution.

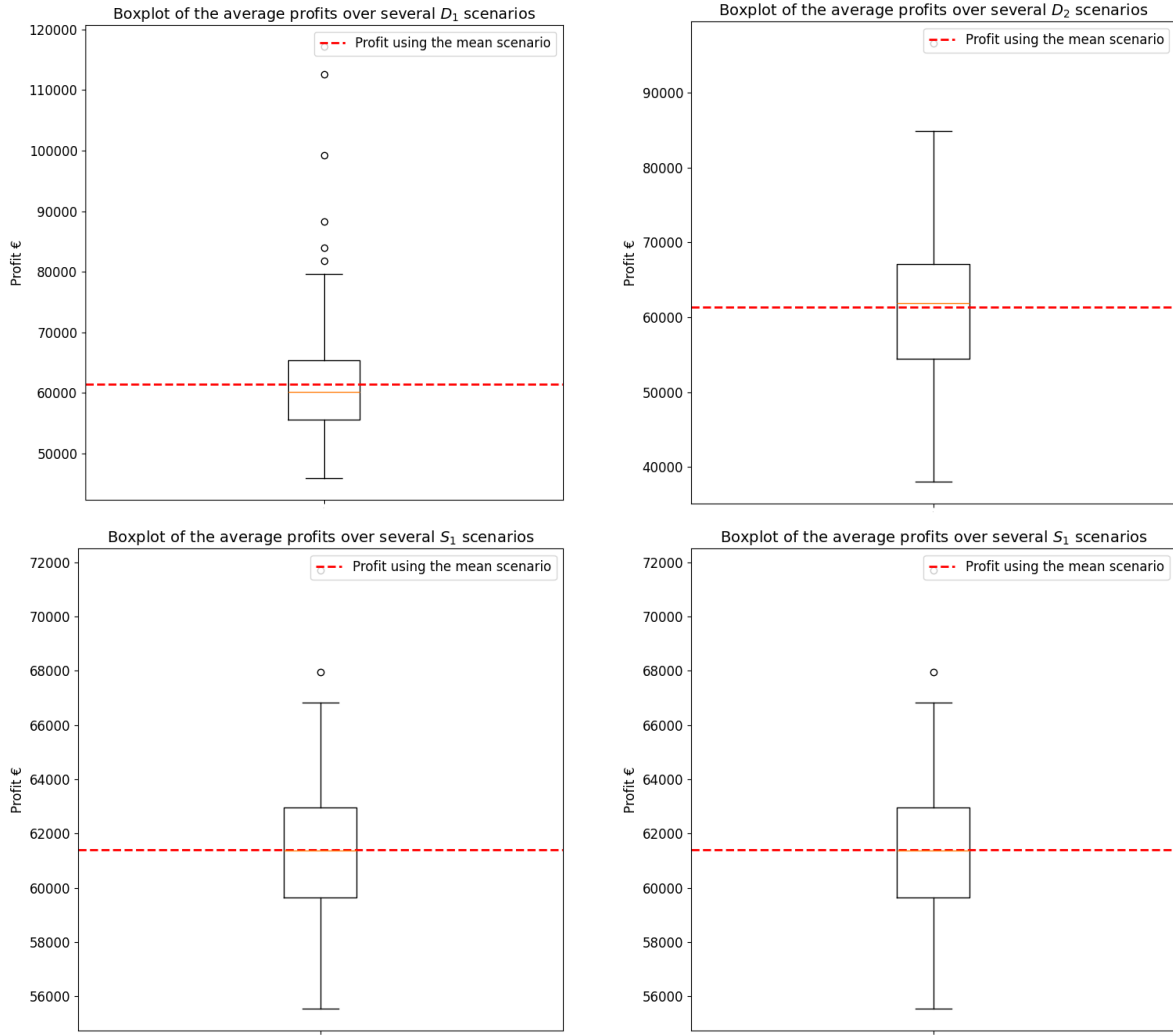


Figure 41: Boxplots of average revenues. The top-left plot shows revenues when D_1 varies while S_1 , S_2 , and D_2 are fixed; the top-right plot shows revenues when D_2 varies; the bottom-left plot shows revenues when S_1 varies; and the bottom-right plot shows revenues when S_2 varies. Each case is evaluated across 100 generated scenarios and computed over 10 000 samples of X . The red dotted line indicates the average profit obtained using the average generated curve.

Appendix A. Fuel prices computation

The short-run marginal cost of electricity generation from fuel F in [EUR/MWh] is computed by the formula

$$C_F = P_F h_F + e_F \tau_{CO_2},$$

where

- P_F is the commodity price of fuel F (e.g. EUR/ton for coal, EUR/barrel for oil, or EUR/MWh for gas),
- h_F is the heat rate (units of fuel input per MWh of energy output),
- e_F is the CO₂ emission factor in [tCO₂/MWh],

- τ_{CO_2} is the CO₂-tax in [EUR/tCO₂].

For example, the coal-based cost becomes

$$C_{\text{coal}} = P_{\text{coal}} \times 0.42 + 0.986 \tau_{CO_2}.$$

The τ_{CO_2} is obtained from <https://www.rte-france.com/en/eco2mix/co2-emissions>, while the fuel prices are extracted from <https://www.investing.com>. The thermal coal is priced using the API2 CIF ARA, quoted in USD per tonne. The oil is priced using the Brent Blend, quoted in USD per barrel. The gas is priced using the Dutch Title Transfer Facility (TTF), quoted in EUR per MWh of energy in gas. As for the heat rates, we select an efficiency of 0.42, 1.5, and 2.4 for Coal, Oil, and Gas, respectively.

Acknowledgements

We thank Peter Tankov (CREST, ENSAE) and Roxana Dumitrescu (CREST, ENSAE) for insightful comments on an earlier draft of this paper. This study was carried out in the framework of “Energy for Climate” interdisciplinary research center and was supported financially by the “Decarbonize energy” program of the Institut Polytechnique de Paris, as well as by the FIME Research Initiative of the Europlace Institute of Finance.

Data availability

This study uses the following data sources:

- *Copernicus Climate Change Service ERA5* (via the Climate Data Store): public meteorological data.
- *EPEX SPOT* day-ahead market data (prices, volumes, aggregated curves): proprietary, obtained under a commercial license.
- *ENTSO-E* day-ahead load forecasts: public, via the ENTSO-E Transparency Platform.
- *Fuel prices* (natural gas, coal, oil): collected from *Investing.com*.
- *French CO₂ tax trajectory*: published by *RTE*.

ERA5, ENTSO-E, Investing.com, and RTE data are publicly accessible (free registration may be required). EPEX SPOT data are proprietary and cannot be redistributed by the authors; equivalent access can be obtained directly from EPEX SPOT/EEX under their licensing terms.

Declaration of generative AI and AI-assisted technologies in the manuscript preparation process During the preparation of this work the authors used ChatGPT in order to assist in language editing, rewriting paragraphs for clarity, and retrieving bibliographic information from publicly available sources. After using this tool/service, the authors reviewed and edited the content as needed and take full responsibility for the content of the published article.

References

Aazami, R., Heydari, O., Tavoosi, J., Shirkhani, M., Mohammadzadeh, A., Mosavi, A., 2022. Optimal Control of an Energy-Storage System in a Microgrid for Reducing Wind-Power Fluctuations. *Sustainability* 14, 6183. URL: <https://www.mdpi.com/2071-1050/14/10/6183>, doi:10.3390/su14106183.

Agrawal, S., Ding, Y., Saberi, A., Ye, Y., 2010. Correlation robust stochastic optimization, in: Proceedings of the twenty-first annual ACM-SIAM symposium on Discrete Algorithms, SIAM. pp. 1087–1096.

Agrawal, S., Ding, Y., Saberi, A., Ye, Y., 2012. Price of correlations in stochastic optimization. *Operations Research* 60, 150–162.

Anderson, E.J., 2013. On the existence of supply function equilibria. *Mathematical Programming* 140, 323–349. URL: <http://link.springer.com/10.1007/s10107-013-0691-7>, doi:10.1007/s10107-013-0691-7.

Aneiros, G., Vilar, J.M., Cao, R., San Roque, A.M., 2013. Functional prediction for the residual demand in electricity spot markets. *IEEE Transactions on Power Systems* 28, 4201–4208.

Baldick, R., Grant, R., Kahn, E., 2004. Theory and Application of Linear Supply Function Equilibrium in Electricity Markets. *Journal of Regulatory Economics* 25, 143–167. URL: <https://link.springer.com/10.1023/B:REGE.0000012287.80449.97>, doi:10.1023/B:REGE.0000012287.80449.97.

Barbry, A., Anjos, M.F., Delage, E., Schell, K.R., 2019. Robust self-scheduling of a price-maker energy storage facility in the new york electricity market. *Energy Economics* 78, 629–646.

Barlow, M.T., 2002. A diffusion model for electricity prices. *Mathematical finance* 12, 287–298.

BIELEWSKI, M., PFRANG, A., BOBBA, S., KRONBERGA, A., GEORGAKAKI, A., LETOUT, S., KUOKKANEN, A., MOUNTRAKI, A., INCE, E., SHTJEFNI, D., et al., 2022. Clean energy technology observatory: Batteries for energy storage in the european union–2022 status report on technology development, trends, value chains and markets. JRC Technical Report / Publications Office of the European Union .

Biggins, F., Ejeh, J.O., Brown, S., 2022. Going, going, gone: Optimising the bidding strategy for an energy storage aggregator and its value in supporting community energy storage. *Energy Reports* 8, 10518–10532.

Buzoianu, M., Brockwell, A., Seppi, D., 2005. A dynamic supply-demand model for electricity prices. Carnegie Mellon University .

Canale, A., Vantini, S., 2016. Constrained functional time series: Applications to the italian gas market. *International Journal of Forecasting* 32, 1340–1351.

Capel, E.H., Dumas, J., 2023. Denoising diffusion probabilistic models for probabilistic energy forecasting, in: 2023 IEEE Belgrade PowerTech, IEEE. pp. 1–6.

Chen, T., Guestrin, C., 2016. Xgboost: A scalable tree boosting system, in: Proceedings of the 22nd ACM SIGKDD international conference on knowledge discovery and data mining, pp. 785–794.

Ciarreta, A., Martinez, B., Nasirov, S., 2023. Forecasting electricity prices using bid data. *International Journal of Forecasting* 39, 1253–1271.

Collet, J., Féron, O., Tankov, P., 2017. Optimal management of a wind power plant with storage capacity, in: Forecasting and risk management for renewable energy. Springer, pp. 229–246.

Commission de Régulation de l’Énergie (CRE), 2022. Analyse des prix de l’électricité du 4 avril 2022. Technical Report. Commission de Régulation de l’Énergie (CRE). Available at https://www.cre.fr/fileadmin/Documents/Rapports_et_etudes/import/Rapport_pic_prix_4avril2022-en.pdf.

Ding, H., Pinson, P., Hu, Z., Wang, J., Song, Y., 2017. Optimal offering and operating strategy for a large wind-storage system as a price maker. *IEEE Transactions on Power Systems* 32, 4904–4913.

Dumitrescu, R., Silvente, R., Tankov, P., 2024. Price impact and long-term profitability of energy storage. *arXiv preprint arXiv:2410.12495* .

Foronda-Pascual, D., Alonso, A.M., 2023. Prediction of matching prices in electricity markets through curve representation. *Energies* 16, 7812.

Galichon, A., 2016. *Optimal Transport Methods in Economics*. Princeton University Press.

Ghelasi, P., Ziel, F., 2024. Hierarchical forecasting for aggregated curves with an application to day-ahead electricity price auctions. *International Journal of Forecasting* 40, 581–596.

Guo, H., Chen, Q., Zheng, K., Xia, Q., Kang, C., 2021. Forecast aggregated supply curves in power markets based on lstm model. *IEEE Transactions on Power Systems* 36, 5767–5779. doi:10.1109/TPWRS.2021.3079923.

Haben, S., Caudron, J., Verma, J., 2021. Probabilistic day-ahead wholesale price forecast: A case study in great britain. *Forecasting* 3, 596–632.

Han, Y., Razaviyayn, M., Xu, R., 2024. Neural network-based score estimation in diffusion models: Optimization and generalization. *arXiv preprint arXiv:2401.15604* .

Ho, J., Jain, A., Abbeel, P., 2020. Denoising diffusion probabilistic models. *Advances in neural information processing systems* 33, 6840–6851.

Holmberg, P., 2008. Unique supply function equilibrium with capacity constraints. *Energy Economics* 30, 148–172. URL: <https://linkinghub.elsevier.com/retrieve/pii/S0140988306001216>, doi:10.1016/j.eneco.2006.10.005.

Holmberg, P., Newbery, D., 2010. The supply function equilibrium and its policy implications for wholesale electricity auctions. *Utilities Policy* 18, 209–226.

Jacobsen, M., 2006. Point process theory and applications: marked point and piecewise deterministic processes. Springer.

Kazmi, H., Tao, Z., 2022. How good are tso load and renewable generation forecasts: Learning curves, challenges, and the road ahead. *Applied Energy* 323, 119565.

Klemperer, P.D., Meyer, M.A., 1989. Supply Function Equilibria in Oligopoly under Uncertainty. *Econometrica* 57, 1243. URL: <https://www.jstor.org/stable/1913707?origin=crossref>, doi:10.2307/1913707.

Knaut, A., Paulus, S., 2016. Hourly price elasticity pattern of electricity demand in the German day-ahead market. Technical Report. EWI working paper.

Kulakov, S., 2020. X-model: further development and possible modifications. *Forecasting* 2, 20–35.

Lewis, P.W., Shedler, G.S., 1979. Simulation of nonhomogeneous poisson processes by thinning. *Naval research logistics quarterly* 26, 403–413.

Li, S., Xiong, H., Chen, Y., 2024. Diffcharge: Generating ev charging scenarios via a denoising diffusion model. *IEEE Transactions on Smart Grid* .

Li, Z., Alonso, A.M., Pascual, L., 2025. Predicting electricity supply and demand curves with functional data techniques. *International Journal of Electrical Power & Energy Systems* 166, 110561.

Lin, N., Palensky, P., Vergara, P.P., 2024. Energydiff: Universal time-series energy data generation using diffusion models. *arXiv preprint arXiv:2407.13538* .

Machlev, R., Zargari, N., Chowdhury, N., Belikov, J., Levron, Y., 2020. A review of optimal control methods for energy storage systems - energy trading, energy balancing and electric vehicles. *Journal of Energy Storage* 32, 101787. URL: <https://linkinghub.elsevier.com/retrieve/pii/S2352152X20316248>, doi:10.1016/j.est.2020.101787.

Mercier, T., Olivier, M., De Jaeger, E., 2023. The value of electricity storage arbitrage on day-ahead markets across europe. *Energy Economics* 123, 106721.

Mitridati, L., Pinson, P., 2017. A bayesian inference approach to unveil supply curves in electricity markets. *IEEE Transactions on Power Systems* 33, 2610–2620.

Peyré, G., 2025. Optimal transport for machine learners. URL: <https://arxiv.org/abs/2505.06589>, [arXiv:2505.06589](https://arxiv.org/abs/2505.06589).

Peyré, G., Cuturi, M., 2019. Computational optimal transport. *Foundations and Trends in Machine Learning* 11, 355–607.

Preger, Y., Barkholtz, H.M., Fresquez, A., Campbell, D.L., Juba, B.W., Romà-Kustas, J., Ferreira, S.R., Chalamala, B., 2020. Degradation of commercial lithium-ion cells as a function of chemistry and cycling conditions. *Journal of The Electrochemical Society* 167, 120532.

Shafiee, S., Zamani-Dehkordi, P., Zareipour, H., Knight, A.M., 2016. Economic assessment of a price-maker energy storage facility in the alberta electricity market. *Energy* 111, 537–547.

Shah, I., Lisi, F., 2020. Forecasting of electricity price through a functional prediction of sale and purchase curves. *Journal of Forecasting* 39, 242–259.

Sinha, N., Lucheroni, C., 2025. Demand and supply curve forecasting using a monotonic autoencoder for short-term day-ahead electricity market bid curves. *Applied Energy* 397, 126262.

Soloviova, M., Vargiolu, T., 2020. Efficient representation of supply and demand curves on day-ahead electricity markets. *arXiv preprint arXiv:2002.00507* .

Song, Y., Sohl-Dickstein, J., Kingma, D.P., Kumar, A., Ermon, S., Poole, B., 2021. Score-based generative modeling through stochastic differential equations, in: *International Conference on Learning Representations*, pp. 1–36. URL: <https://openreview.net/forum?id=PxTIG12RRHS>.

Zhang, S., Cheng, Y., Yu, N., 2024. Generating synthetic net load data with physics-informed diffusion model. *arXiv preprint arXiv:2406.01913* .

Ziel, F., Steinert, R., 2016. Electricity price forecasting using sale and purchase curves: The x-model. *Energy Economics* 59, 435–454.